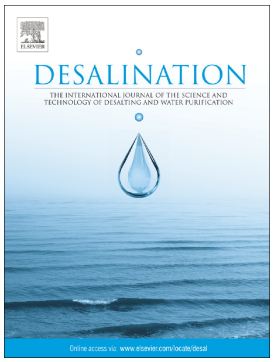

Study of seawater droplet impacting and freezing coupling processes with combined phase-field and multi-relaxation-time lattice Boltzmann method

Xinyu Liu, Han Yuan, Yuan Zhao, Ji Zhang, Haibin Wang

PII: S0011-9164(25)00163-8

DOI: https://doi.org/10.1016/j.desal.2025.118688

Reference: DES 118688

To appear in: *Desalination*

Received date: 23 December 2024

Revised date: 31 January 2025

Accepted date: 10 February 2025

Please cite this article as: X. Liu, H. Yuan, Y. Zhao, et al., Study of seawater droplet impacting and freezing coupling processes with combined phase-field and multi-relaxation-time lattice Boltzmann method, *Desalination* (2024), https://doi.org/10.1016/j.desal.2025.118688

Study of seawater droplet impacting and freezing coupling processes with combined phase-field and multi-relaxation-time lattice Boltzmann method

Xinyu Liu[a], Han Yuan[a,*], Yuan Zhao[a], Ji Zhang[a], Haibin Wang[b]

a. College of Engineering, Ocean University of China, Qingdao 266100, China

b. Department of Naval Architecture, Ocean and Marine Engineering, University of Strathclyde, Glasgow G4 0LZ, UK

Abstract

The phenomenon of seawater droplets impacting on low-temperature surface and freezing is ubiquitous in the field of marine engineering. An integrated phase field and multi-relaxation lattice Boltzmann method is employed in this paper to simulate the freezing behavior of seawater droplet impacting on low-temperature surface. The model can describe changes in the solid-liquid-gas three-phase interface, and obtain the concentration, temperature and velocity distribution inside the droplet. According to the simulation results, the droplet no longer retracts after impacting the surface due to the bottom solidification. A clear solid-liquid interface can be observed within the droplet. Above the solid-liquid interface, there is a high-concentration brine film. Below the salt water film, the frozen droplet exhibits a distinctly dendritic structure with plenty of high concentration brine pockets. Meanwhile, the effects of surface wettability, impacting velocity, surface temperature and initial salinity on dynamic factors and freezing efficiency are investigated. The results indicate that reducing surface wettability is beneficial for anti-icing, and the morphology of frozen droplet changes from central-pointy to central-concave with the increase of contact angle. When the time step is 25000$\triangle t$, the freezing efficiency at θ=60° and 150° are 98.35% and 84.48%, respectively. Additionally, a drop in surface temperature leads to salt solution enrichment between dendrites. As the surface temperature drops from -10°C to -20°C, the max concentration inside the droplet increases from 0.108kg/kg to 0.216kg/kg. The current study serves to provide guidance for the development of anti-icing on the surface of marine structures and seawater freezing desalination by precisely revealing the coupling mechanism of droplet impact and seawater freezing.

Keywords: seawater droplet impact; freezing paradigm; phase field method; lattice Boltzmann method; multi-physical field coupling

Highlights

(1) Seawater droplet impacting and freezing coupling processes is simulated in mesoscale.

(2) A combined phase-field and multi-relaxation-time lattice Boltzmann method is developed.

(3) Multi-physical field coupling and multiscale simulation method is conducted.

(4) Effects of droplet and surface parameters on impacting-freezing characteristics are investigated.

1. Introduction

The phenomenon of seawater droplets impacting and freezing on cold surfaces commonly exists in marine engineering within middle and high-latitude regions. This icing-related occurrence poses significant challenges to the structural safety and operational stability of various facilities, such as ships [1], offshore platforms [2], and wind turbine blades [3]. The accumulation of ice can lead to increased weight, altering mechanical and aerodynamic characteristics of equipment [4]. Additionally, the presence of saline solutions can accelerate structural corrosion, resulting in safety hazards [5]. Conversely, there are beneficial applications, such as freezing desalination (FD) [6] and cold thermal energy storage materials [7], which leverage the properties of seawater freezing for innovative solutions. The freezing desalination method is noted for its economic viability and reduced susceptibility to common challenges in desalination processes, particularly due to the lower latent heat of solidification and diminished risk of corrosion at lower operating temperatures [8]. Despite the above advantages, freezing desalination has not been widely used in commercial owing to its low desalting rate. Barma et al. [9] investigated the performance of the drop-based FD and found that the salinity reduction rate can be increased to 72%. Therefore, studying the freezing behavior of seawater droplets is critical for advancing technologies associated with freezing desalination and anti-icing strategies.

The impact of seawater droplet on cold surface typically involves two physical processes: impacting and solidification. Hence, this section will focus on a review of relevant research works from the aspects of the dynamic characteristics of droplet impact, the freezing characteristics of seawater, and the coupled processes of droplet impacting and freezing.

Research into droplet impacting on dry solid surfaces has revealed various phenomena such as spreading, splashing, receding, and rebounding [10]. These dynamics play crucial roles in numerous industrial applications, prompting extensive studies through experimental, theoretical, and numerical approaches. For instance, experiments primarily observe changes in droplet morphology during motion,

capturing the flow of the free surface and the behavior of the gas-liquid-solid contact line. Chen et al. [11] experimentally studied droplet dynamics at varying impact velocities, concluding that splashing occurs when droplet velocity exceeds a critical threshold, resulting in the formation of multiple smaller droplets. Asai et al. [12] systematically explored the effects of surface wettability on droplet behavior, concluding that different interactions, such as spreading and recoiling, manifest on hydrophilic and hydrophobic surfaces.

While experimental studies effectively document droplet impact phenomena, understanding the underlying mechanisms is more complex. To address this, various numerical methods, including PIC (Particle in Cell), VOF (Volume of Fluid) [13] and Level-set approaches, have been developed to capture phase interface dynamics. However, traditional CFD (Computational Fluid Dynamics) approaches often struggle with accurately tracking all phase interfaces during droplet deformation. Recent advancements include the use of the LBM (lattice Boltzmann method), which simulates phase interactions with greater accuracy. Raman et al. [14] applied a phase-field LBM to explore the impact of contact angle on droplet recoiling behavior, finding that increasing receding contact angles decrease spreading factors and shift behavior from deposition to rebounding. Other studies [15-17] have utilized multiphase LBM method to examine the interplay between the spreading factor and contact time relative to dimensionless numbers such as Weber number *We*, Reynolds number *Re* and Ohnesorge number *Oh* et al.

The process of seawater freezing involves the solidification of seawater into sea ice, guided by classical nucleation theory [18]. When nucleation free energy surpasses Gibbs free energy, heterogeneous nucleation occurs at solid-liquid or solid-gas-liquid interfaces, with the solid-gas-liquid interface being the predominant site. Notably, unlike pure water, the freezing of seawater is complex due to concurrent heat and mass transfer processes. This complexity leads to discrepancies between phase change rates and ion migration, resulting in high-concentration brine pockets and salt channels within the ice structure[19]. Zhao et al. [20] employed molecular dynamics simulations to reveal nanoscale mechanisms influencing seawater freezing, identifying that increased subcooling or decreased salt concentration lower interfacial free energy, thereby enhancing the propagation rate of the freezing front. Meanwhile, in the study of sessile seawater droplet freezing, Zhao et al. [21] further proves that both the nucleation time and freezing time will be reduced by the decreasing salinity or temperature. Additionally, Eghtesad et al. [22] utilized CFD modeling to investigate the freezing

process of static seawater on a macroscopic scale, noting that increased heat flux rates enhance freezing rates while contributing to substantial salt enrichment in the ice layer.

Microscopic studies provide valuable insights into the atomic and molecular behavior of seawater during the freezing process, while macroscopic studies offer a direct view of the overall evolution characteristics of the ice layer. Understanding the growth and differentiation of ice crystals, as well as the pathways for salt transfer, is critical to comprehending the freezing behavior of seawater. The phase field model, which is grounded in Ginzburg-Landau theory [23], effectively captures these processes. By introducing an order parameter, the model transitions from a sharp liquid-solid interface to a diffuse interface, thereby eliminating the necessity to explicitly differentiate between phases and interfaces. This approach enables an accurate simulation of dendritic growth during the freezing of sea ice. Demange et al. [24] developed a modified phase-field model that incorporates surface diffusion and anisotropy effects to predict ice crystal growth. Their simulations revealed 15 distinct snowflake morphologies by varying kinetic parameters. Furthermore, several studies [25-28] have been conducted to explore the mechanisms governing ice crystal growth and the formation of brine pockets within sea ice. By incorporating factors such as phase change, solute migration, heat transfer, and fluid flow into their analyses, researchers concluded that the competition among dendrites is a primary factor driving solute enrichment at the solid-liquid interface.

Over the past few decades, the complexity of droplet impacting and freezing phenomenon has been a barrier to experimental and numerical investigations. The findings available primarily reveal two distinct morphologies of completely frozen droplets: the central-pointy pattern [29] and the central-concave pattern [30, 31]. Shang et al. [32] explored the freezing morphology of droplets under high impact velocities, noting that as the impact speed increases, the freezing pattern transitions from a central-pointy structure to an annular icing form. Additionally, various experimental studies have examined factors such as the inclination angle [33] and surface hydrophilicity [34], which influence the interactions between droplet dynamics and crystallization. Lin et al. [35] recorded the morphologies of seawater droplet impacting on ice surface. They discovered that a number of small protrusions appear on the top of the frozen brine droplet, and with the rise of salt concentration, the number of protrusions gets diminish. Besides, in terms of simulation approaches, methods such as the VOF (Volume of Fluid) method [36] and the LBM method [37] combined with solid-liquid phase change models are predominant. Subcooling is identified as a driving force behind the freezing process. For instance,

Zhang et al. [38] simulated the freezing morphologies of impacting water droplets on ultra-cold surfaces ranging from -50°C to -100°C using the VOF method. They concluded that an increase in *We* number and a decrease in surface temperature both contribute to a shift in freezing patterns from a central-pointy to a central-concave configuration.

The freezing process of seawater droplets is intricately characterized by several key factors, including the hydrodynamics of the droplets (such as velocity and diameter), the physics governing the droplets (including temperature and concentration), and the properties of the substrate (temperature, wettability, and surface roughness). The complex interactions among these parameters give rise to varied freezing structures. As shown in Fig. 1 A, Chu et al. [39] observed the presence of brine film on the top of the fixed frozen seawater droplet, and the ice crystals will sprout from the liquid interface and continue to grow up. Meanwhile, according to Fig. 1B, Fang et al. [33] studied the freezing behavior of impacting water droplet, and found that different substrate temperature will result in different shape of dendrites in the freezing front.

Although the dynamics of a droplet impacting on solid surface at ambient temperature have been extensively studied, the mechanism of a seawater droplet impact on low-temperature surface and subsequently freeze remains less understood. The dynamics of the moving droplet are significantly influenced by the freezing process, and the phase change and mass transfer processes occurring within the seawater droplets are equally affected by the droplet's kinetic parameters. To address these challenges, Section 2 introduces a coupled phase-field and multi-component lattice Boltzmann method aimed at tracking the solid-liquid-gas interface during the impacting and freezing processes of seawater droplets (see Fig. 1C). Section 3 presents a new numerical simulation method that couples multiple physical fields and employs multiscale calculation techniques. In Section 4, the research explores how droplet dynamic parameters and thermodynamic conditions affect freezing morphology, the growth of internal ice crystals, and salt diffusion processes at the mesoscopic scale.

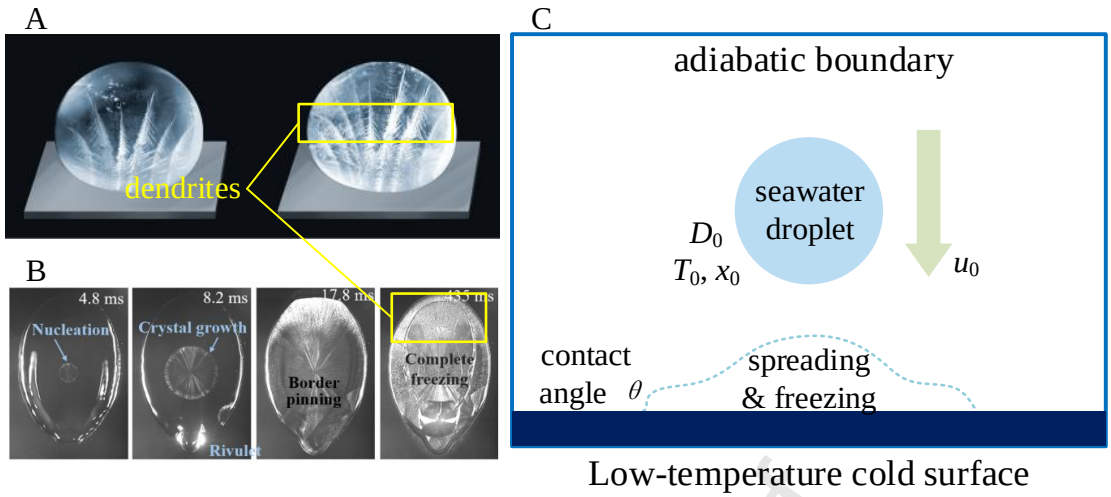

Fig. 1 Schematic of droplet freezing. A. Morphology of seawater droplet freezing in steady state [39]. B. Snapshots of a water droplet impacting on inclined substrate [33]. C. Schematic illustration of seawater droplet impact on a low-temperature cold surface.

2. Mathematical modelling

Seawater droplet impacting on cold surface and freezing is a complex multiphase liquid-solid-gas coupling problem, which is accompanied by gas-liquid interface tracking, solid-liquid phase change, solute migration and heat transfer. Multi-component and multi-relaxation-time pseudopotential lattice Boltzmann method is applied to obtain the interface between liquid and gas phases. Meanwhile, phase field method is introduced to describe the process of ice crystal growth and salt migration. The seawater droplet impacting and freezing coupling processes are calculated through parameter transfer between various physical fields.

2.1 Multi-component and multi-relaxation-time (MRT) pseudopotential lattice Boltzmann method.

Considering the numerical stability, the multi-relaxation-time (MRT) pseudopotential lattice Boltzmann method is conducted to simulate the impact process of seawater droplet. In the distributed velocity space, the evolution equation can be expressed as:

$$f_{\sigma,\alpha}\left(x+\mathbf{e}_\alpha\delta_t,t+\delta_t\right)-f_{\sigma,\alpha}(x,t)=-\left(\mathbf{M}^{-1}\mathbf{\Lambda}\mathbf{M}\right)_{\alpha\beta}\left[f_{\sigma,\beta}(x,t)-f_{\sigma,\beta}^{(eq)}(x,t)\right] \quad (1)$$

in which, $f_{\sigma,\alpha}(x,t)$ represents the density distribution function of component σ at the position x and time t. δ_t and $f_{\sigma,\beta}^{(eq)}(x,t)$ denote the time step, density ρ equilibrium distribution function. $\left(\mathbf{M}^{-1}\mathbf{\Lambda}\mathbf{M}\right)_{\alpha\beta}$ refers to collision matrix, in which $\mathbf{M}$ and $\mathbf{\Lambda}$ are orthogonal transformation matrix and the diagonal relaxation matrix, respectively.

D2Q9 lattice scheme is adopted in the two-dimensional simulation, and the discrete velocities $\mathbf{e}_\alpha$ is deemed as:

$$\mathbf{e}_\alpha = \left(\mathbf{e}_{\alpha x}, \mathbf{e}_{\alpha y}\right)^{\mathrm{T}} = c\begin{bmatrix} 0 & 1 & 0 & -1 & 0 & 1 & -1 & -1 & 1 \\ 0 & 0 & 1 & 0 & -1 & 1 & 1 & -1 & -1 \end{bmatrix} \tag{2}$$

The basis vector of the transformation matrix is written as [40]:

$$\begin{aligned} &\varphi_{0,\alpha} = 1; \quad \varphi_{1,\alpha} = 3\left(\mathbf{e}_{\alpha x}^2 + \mathbf{e}_{\alpha y}^2\right) - 4; \quad \varphi_{2,\alpha} = 4 - \frac{21}{2}\left(\mathbf{e}_{\alpha x}^2 + \mathbf{e}_{\alpha y}^2\right) + \frac{9}{2}\left(\mathbf{e}_{\alpha x}^2 + \mathbf{e}_{\alpha y}^2\right)^2 \\ &\varphi_{3,\alpha} = \mathbf{e}_{\alpha x}; \quad \varphi_{4,\alpha} = \left[3\left(\mathbf{e}_{\alpha x}^2 + \mathbf{e}_{\alpha y}^2\right) - 5\right]\mathbf{e}_{\alpha x}; \quad \varphi_{5,\alpha} = \mathbf{e}_{\alpha y} \\ &\varphi_{6,\alpha} = \left[3\left(\mathbf{e}_{\alpha x}^2 + \mathbf{e}_{\alpha y}^2\right) - 5\right]\mathbf{e}_{\alpha y}; \quad \varphi_{7,\alpha} = \mathbf{e}_{\alpha x}^2 - \mathbf{e}_{\alpha y}^2; \quad \varphi_{8,\alpha} = \mathbf{e}_{\alpha x}\mathbf{e}_{\alpha y} \end{aligned} \tag{3}$$

Thus, the transformation matrix **M** can be derived as:

$$\mathbf{M} = \begin{bmatrix} 1 & 1 & 1 & 1 & 1 & 1 & 1 & 1 & 1 \\ -4 & -1 & -1 & -1 & -1 & 2 & 2 & 2 & 2 \\ 4 & -2 & -2 & -2 & -2 & 1 & 1 & 1 & 1 \\ 0 & 1 & 0 & -1 & 0 & 1 & -1 & -1 & 1 \\ 0 & -2 & 0 & 2 & 0 & 1 & -1 & -1 & 1 \\ 0 & 0 & 1 & 0 & -1 & 1 & 1 & -1 & -1 \\ 0 & 0 & -2 & 0 & 2 & 1 & 1 & -1 & -1 \\ 0 & 1 & -1 & 1 & -1 & 0 & 0 & 0 & 0 \\ 0 & 0 & 0 & 0 & 0 & 1 & -1 & 1 & -1 \end{bmatrix} \tag{4}$$

Besides, the diagonal relaxation matrix $\mathbf{\Lambda}$ is written as:

$$\Lambda = diag\left(\tau_c^{-1}, \tau_e^{-1}, \tau_\xi^{-1}, \tau_c^{-1}, \tau_q^{-1}, \tau_c^{-1}, \tau_q^{-1}, \tau_v^{-1}, \tau_v^{-1}\right) \tag{5}$$

where τ_c is set to 1.0, and τ_ξ and τ_q have the value of 1.1. Besides, the value of τ_e and τ_v are related to the bulk viscosity μ_{B} and kinematic viscosity μ, respectively.

$$\mu_{\mathrm{B}} = \rho c_{\mathrm{s}}^2\left(\tau_v - 0.5\right)\delta_{\mathrm{t}} \tag{6}$$

$$\mu = \rho c_{\mathrm{s}}^2\left(\tau_e - 0.5\right)\delta_{\mathrm{t}} \tag{7}$$

Moreover, according to the transformation matrix, the evolution equation that introduces the force term and surface tension can be rewritten as:

$$\mathbf{m}^* = \mathbf{m} - \mathbf{\Lambda}\left(\mathbf{m} - \mathbf{m}^{eq}\right) + \delta_{\mathrm{t}}\left(\mathbf{I} - \frac{\mathbf{\Lambda}}{2}\right)\bar{\mathbf{S}} + \delta_{\mathrm{t}}\mathbf{C} \tag{8}$$

in which, **I** means the unit tensor, **m** and $\mathbf{m}^*$ are moment function and equilibrium moment function.

$$\mathbf{m} = \mathbf{M}\boldsymbol{f} = \left(m_0, m_1, \cdots, m_{N-2}, m_{N-1}\right)^{\mathrm{T}} = \mathbf{M}\left(f_0, f_1, \cdots, f_{N-2}, f_{N-1}\right)^{\mathrm{T}} \tag{9}$$

$$\mathbf{m}^{\mathrm{eq}} = \mathbf{M}\boldsymbol{f}^{\mathrm{eq}} = \rho\left(1,-2+3u^2,1-3u^2,u_x,-u_x,u_y,-u_y,u_x^2-u_y^2,u_xu_y\right)^T \tag{10}$$

The streaming process can be written as:

$$f_{\sigma,\alpha}\left(x+\mathbf{e}_\alpha\delta_t,t+\delta_t\right) = f^*_{\sigma,\alpha}(x,t) = \mathbf{M}^{-1}\mathbf{m}^* \tag{11}$$

In the pseudopotential model, the interaction potential that coupled with non-ideal state equation is introduced to describe the interactions between fluid particles. According to Shan-Chen model, the interaction pseudopotential force in the multi-component system is described as [17]:

$$\mathbf{F}_{\sigma,\mathrm{int}}(x,t) = -G_{\sigma\sigma}\psi_\sigma(x)\sum_{\alpha=0}^{N-1}w\left(\left|\mathbf{e}_\alpha\right|^2\right)\psi_\sigma\left(x+\mathbf{e}_\alpha\delta t\right)\mathbf{e}_\alpha - G_{\sigma\bar{\sigma}}\psi_\sigma(x)\sum_{\alpha=0}^{N-1}w\left(\left|\mathbf{e}_\alpha\right|^2\right)\psi_{\bar{\sigma}}\left(x+\mathbf{e}_\alpha\delta t\right)\mathbf{e}_\alpha \tag{12}$$

where G represents the interaction strength, ψ is pseudopotential potential, $w\left(\left|\mathbf{e}_\alpha\right|^2\right)$ stands for weights, and in the D2Q9 model, the value is given by $w(0)=0$, $w(1)=1/3$ and $w(2)=1/12$.

Moreover, in order to improve the model stability and keep a good thermodynamic consistency, the interaction force of water is modified as [41]:

$$\mathbf{F}_{\sigma\sigma,\mathrm{int}}(x,t) = -\beta G_{\sigma\sigma}\psi_\sigma(x)\sum_{\alpha=0}^{N-1}w\left(\left|\mathbf{e}_\alpha\right|^2\right)\psi_\sigma\left(x+\mathbf{e}_\alpha\delta t\right)\mathbf{e}_\alpha - \frac{1-\beta}{2}G_{\sigma\sigma}\sum_{\alpha=0}^{N-1}w\left(\left|\mathbf{e}_\alpha\right|^2\right)\left(\psi_\sigma\left(x+\mathbf{e}_\alpha\delta t\right)\right)^2\mathbf{e}_\alpha \tag{13}$$

in which, β is the adjusting parameters, which is set as 1.25.

Meanwhile, as seawater solidifies into sea ice, the fluid-solid interaction force between the fluid and the ice crystal $F_{\sigma s}$ is also taken into consideration [42].

$$\mathbf{F}_{\sigma s}(x,t) = -G_{\sigma s}\psi_\sigma(x)\sum_{\alpha=0}^{N-1}w\left(\left|\mathbf{e}_\alpha\right|^2\right)s_\sigma\left(x+\mathbf{e}_\alpha\delta t\right)\mathbf{e}_\alpha \tag{14}$$

where $G_{\sigma s}$ refers to the adsorption parameter, s_σ denotes an indicator function, and it takes on the value of $s(x)=0$ in the fluid phase and $s(x)=1$ in the crystallized phase [43].

In present article, the components of seawater and air are defined with the subscript of 1 and 2, respectively. According to Ref. [44] and [45], the interaction potential for liquid water and air components is calculated as follows and modified by a constant value of 0.125 (defined as δ).

$$\psi_1 = \sqrt{\frac{2\left(p_{\mathrm{EOS}}-\rho_1 c_s^2\right)}{G_{11}c_s^2}} \tag{15}$$

$$\psi_2 = \rho_2 \tag{16}$$

in which, p_{EOS} stands for a thermodynamic equation of state (EOS), and in this simulation the

Peng-Robinson (PR) EOS is adopted:

$$p_{\mathrm{EOS}} = \frac{\rho_1 RT}{1-b\rho_1} - \frac{a\alpha(T)\rho_1^2}{1+2b\rho_1 - b^2\rho_1^2} \tag{17}$$

$$a = \left(0.457235R^2T_{\mathrm{c}}^2\right)/\ p_{\mathrm{c}} \tag{18}$$

$$b = \left(0.077796RT_{\mathrm{c}}\right)/\ p_{\mathrm{c}} \tag{19}$$

$$\alpha(T) = \left(1+\left(0.37464+1.54226\omega-0.26992\omega^2\right)\left(1-\left(T/T_{\mathrm{c}}\right)^{0.5}\right)\right)^2 \tag{20}$$

where a, b, R, ω, ρ_{c} *and* T_{c} are set as 1/49, 2/21, 1, 0.344, 2.657 and 0.036461, respectively [45]. Besides, c_{s} is the lattice sound speed, which can be obtained by:

$$c_{\mathrm{S}} = c/\sqrt{3} \tag{21}$$

$$c = \delta_x/\delta_t \tag{22}$$

where δ_x stands for the lattice space step.

Moreover, by introducing a virtual layer at the solid boundary, the influence of contact angles on the fluid–solid interaction force can be directly determined through the pseudopotential force of fluids:

$$\rho_{i,0} = \rho_{i,2} + \tan\left(\frac{\pi}{2}-\theta_a\right)\left|\rho_{i+1,1}-\rho_{i-1,1}\right| \tag{23}$$

in which, θ_a is the destined static contact angle.

Based on the pseudopotential force, the forcing term $\bar{\mathbf{S}}$ in the moment space is given by [46]:

$$\bar{\mathbf{S}} = \begin{bmatrix} 0 \\ 6\left(u_xF_x+u_yF_y\right) \\ -6\left(u_xF_x+u_yF_y\right) \\ F_x \\ -F_x \\ F_y \\ -F_y \\ 2\left(u_xF_x-u_yF_y\right) \\ \left(u_xF_y-u_yF_x\right) \end{bmatrix} \tag{24}$$

Besides, the surface tension term **C** in MRT LB equation can be written as [44]:

$$\mathbf{C}=\begin{bmatrix} 0 \\ 1.5\tau_e^{-1}\left(Q_{xx}+Q_{yy}\right) \\ -1.5\tau_\xi^{-1}\left(Q_{xx}+Q_{yy}\right) \\ 0 \\ 0 \\ 0 \\ 0 \\ -\tau_v^{-1}\left(Q_{xx}-Q_{yy}\right) \\ -\tau_v^{-1}Q_{xy} \end{bmatrix} \tag{25}$$

$$\mathbf{Q}=\gamma\frac{G_{11}}{2}\psi(\mathbf{x})\sum_{\alpha}w\left(\left|\mathbf{e}_\alpha\right|^2\right)\left[\psi_1\left(\mathbf{x}+\mathbf{e}_\alpha\right)-\psi_1(\mathbf{x})\right]\mathbf{e}_\alpha\mathbf{e}_\alpha \tag{26}$$

where γ is the surface tension adjusting parameter, and the value is set as 0.5 [44].

The macroscopic density ρ and velocity u of multi-component pseudopotential LB model can be obtained via:

$$\rho_\sigma=\sum_{\alpha=0}^{N-1}f_{\sigma,\alpha} \tag{27}$$

$$\rho_\sigma u_\sigma=\sum_{\alpha=0}^{N-1}\mathbf{e}_\alpha f_{\sigma,\alpha}+\frac{\delta_t}{2}(F_{\sigma,\mathrm{int}}+F_{\sigma\mathrm{s}}) \tag{28}$$

$$u=\sum_{1}^{\sigma}\rho_\sigma u_\sigma\Big/\sum_{1}^{\sigma}\rho_\sigma \tag{29}$$

2.2 Phase field method.

The phase field model is based on the Ginzburg-Landau theory, and a phase field order parameter ϕ is introduced to determine the physical state. The evolution equation of phase field can be determined by:

$$\frac{\partial\phi}{\partial t}=-M\frac{\delta F}{\delta\phi} \tag{30}$$

Where ϕ stands for the phase field variable, which varies between 1 (the solid phase) and 0 (the liquid phase). M is the mobility of the phase field, which is related to the driving force of the interface. F denotes the bulk free energy function.

According to the KKS theory[47], the bulk free energy function F can be written as:

$$F\left(\phi,c,T\right)=\int_\Omega\left[f\left(\phi,c,T\right)+\frac{1}{2}\varepsilon(\mathbf{n})^2\left|\nabla\phi\right|^2+\frac{1}{2}\delta^2\left|\nabla c\right|^2\right]d\Omega \tag{31}$$

in which, c and T represent the concentration and temperature. ε and δ indicate the gradient of the phase

field and concentration field, respectively. Ω is the volume of a closed system.

By substituting the bulk free energy function, the governing equation can be obtained as:

$$\frac{\partial \phi}{\partial t} = M\left[\varepsilon^2 \nabla^2 \phi + \frac{\partial}{\partial x}\left(|\nabla \phi|^2 \varepsilon(\mathbf{n}) \frac{\partial \varepsilon(\theta)}{\partial \phi_x} \right) + \frac{\partial}{\partial y}\left(|\nabla \phi|^2 \varepsilon(\mathbf{n}) \frac{\partial \varepsilon(\theta)}{\partial \phi_y} \right) - f_\phi \right] \tag{32}$$

According to the free energy equation of binary mixture, the free energy density of solid-liquid mixture is obtained as:

$$f(\phi, c, T) = h(\phi) f^{\mathrm{S}}(c_{\mathrm{S}}) + (1 - h(\phi)) f^{\mathrm{L}}(c_{\mathrm{L}}) + Wg(\phi) \tag{33}$$

where the free energy density function *f* consists of the free energy densities of the solid and liquid phases, as well as a double well potential function.

f is the Helmholtz free energy density function, which is defined as:

$$f(\phi, c) = h(\phi) f^{\mathrm{S}}(c_{\mathrm{S}}) + (1 - h(\phi)) f^{\mathrm{L}}(c_{\mathrm{L}}) + Wg(\phi) \tag{34}$$

in which, the superscript and subscript S and L stand for solid and liquid phase.

Thus, f_ϕ can be deduced as:

$$f_\phi(c, \phi) = \frac{\partial f}{\partial \phi} = -h'(\phi)\left[\frac{RT}{V_{\mathrm{m}}} \ln \frac{(1 - c_{\mathrm{S}}^{\mathrm{e}})(1 - c_{\mathrm{L}})}{(1 - c_{\mathrm{L}}^{\mathrm{e}})(1 - c_{\mathrm{S}})} \right] + Wg'(\phi) \tag{35}$$

Moreover, $h(\phi)$ and $g(\phi)$ denote the interpolation function and the double potential well function. *W* is the potential height of the double well potential.

$$h(\phi) = \phi^3 (10 - 15\phi + 6\phi^2) \tag{36}$$

$$g(\phi) = \phi^2 (1 - \phi)^2 \tag{37}$$

An anisotropic function for describing the crystal morphology and interface direction has been deduced based on the six fold horizontal symmetry of snowflakes, which can be governed by [48]:

$$\varepsilon(\mathbf{n}) = \varepsilon_0 (1 + \varepsilon_{\mathrm{xy}} \cos(6\theta)) \tag{38}$$

$$\mathbf{n} = \frac{\nabla \phi}{|\nabla \phi|} \tag{39}$$

in which, **n** refers to local normal vector. θ and ψ represent azimuthal angles.

$$\theta = \arctan\left(\frac{n_{\mathrm{y}}}{n_{\mathrm{x}}} \right) \tag{40}$$

Besides, in order to describe the primary habit of snowflakes [48], the $|\nabla \phi|$ and the Laplace

diffusion term are calculated as:

$$|\nabla\phi| = \sqrt{\phi_x^2 + \phi_y^2} \tag{41}$$

$$\nabla^2\phi = \phi_{xx} + \phi_{yy} \tag{42}$$

Thus, the crystalline anisotropic function can be simplified as:

$$\varepsilon(\mathbf{n}) = \varepsilon_0\left[1 + \varepsilon_{xy}\left(n_x^6 + 15n_x^2n_y^4 - 15n_x^4n_y^2 - n_y^6\right)\right] \tag{43}$$

where ε_0 can be calculated by:

$$\sigma = \frac{\varepsilon_0\sqrt{W}}{3\sqrt{2}} \tag{44}$$

$$2\lambda = \alpha\sqrt{2}\frac{\varepsilon_0}{\sqrt{W}} \tag{45}$$

where λ and σ refer to interface thickness and interface energy, respectively. The value of α is set as 2.2, which is related to the interface thickness.

Besides, the phase field mobility M is given as:

$$M^{-1} = \frac{\varepsilon_0^3}{\sigma\sqrt{2W}}\left[\frac{1}{D(\phi)}\zeta\left(c_L^e, c_S^e\right)\right] \tag{46}$$

in which, ζ is the prescribed distance between the interface and the solute sink in liquid, which is calculated from [47]:

$$\zeta = \frac{RT}{V_m}\left(c_L^e - c_S^e\right)^2\int_0^1 \frac{h(\phi)[1-h(\phi)]}{[1-h(\phi)]c_L^e\left(1-c_L^e\right) + h(\phi)c_S^e\left(1-c_S^e\right)}\cdot\frac{d\phi}{\phi(1-\phi)} \tag{47}$$

2.3 Solute field model

Based on Fick's second law and KKS model, the diffusion equation on solute field c is described in the form of free energy density [47]:

$$\frac{\partial c}{\partial t} + \nabla\bullet(Vc) = \nabla\left(\frac{D(\phi)}{f_{cc}}\nabla f_c\right) \tag{48}$$

in which, $\nabla\bullet(Vc)$ stands for the convection term, which represents the effect of velocity change on concentration transfer during droplet impacting.

The concentration of binary mixed solution at the interface can be written as:

$$c = h(\phi)c_S + \left[1-h(\phi)\right]c_L \tag{49}$$

Meanwhile, in KKS model, the interfacial region is considered as a mixture of solid and liquid with

the same free energy densities.

$$f_{\mathrm{cS}}^{\mathrm{S}}\left[c_{\mathrm{S}}(x,t)\right]=f_{\mathrm{cL}}^{\mathrm{L}}\left[c_{\mathrm{L}}(x,t)\right] \tag{50}$$

where, the interaction between the fraction of solid c_S and liquid c_L phase are defined as:

$$\frac{c_{\mathrm{S}}}{c_{\mathrm{L}}}=\frac{c_{\mathrm{S}}^{\mathrm{e}}}{c_{\mathrm{L}}^{\mathrm{e}}}=k^{e} \tag{51}$$

in which, k^e represents the equilibrium partition coefficient.

Besides, the terms on the right side of the diffusion equation can be simplified according to the theory of dilute solution approximation, and the detailed derivation process can be found from Ref. [49].

D denotes the diffusion coefficient of solutes.

$$D(\phi)=h(\phi)D_S+[1-h(\phi)]D_L \tag{52}$$

where D_S and D_L are the solute diffusion coefficient of solid and liquid phase.

∇f_c represents the first derivative of the free energy density f with respect to the concentration c.

$$\nabla f_c=\nabla f_{\mathrm{c}}^{\mathrm{L}}=f_{\mathrm{cc}}^{\mathrm{L}}\nabla c+f_{\mathrm{c}\phi}^{\mathrm{L}}\nabla\phi \tag{53}$$

Meanwhile, according to the free energy density function f shown in Eq. 31, it can also obtained that:

$$\frac{f_{c\phi}(c,\phi)}{f_{\mathrm{cc}}(c,\phi)}=h'(\phi)\left(c_{\mathrm{L}}-c_{\mathrm{S}}\right) \tag{54}$$

f_{cc} is the second partial derivatives of free energy function.

$$f_{cc}(c,\phi)=\frac{f_{\mathrm{cc}}^{\mathrm{S}}(c_{\mathrm{S}})\,f_{\mathrm{cc}}^{\mathrm{L}}(c_{\mathrm{L}})}{\left(1-h(\phi)\right)f_{\mathrm{cc}}^{\mathrm{S}}(c_{\mathrm{S}})+h(\phi)\,f_{\mathrm{cc}}^{\mathrm{L}}(c_{\mathrm{L}})} \tag{55}$$

where $f_{\mathrm{cc}}^{\mathrm{L}}$ and $f_{\mathrm{cc}}^{\mathrm{S}}$ are deemed as:

$$f_{\mathrm{cc}}^{\mathrm{L}}=\frac{RT}{V_m}\frac{1}{c_{\mathrm{L}}\left(1-c_{\mathrm{L}}\right)} \tag{56}$$

$$f_{\mathrm{cc}}^{\mathrm{S}}=\frac{RT}{V_m}\frac{1}{c_{\mathrm{S}}\left(1-c_{\mathrm{S}}\right)} \tag{57}$$

where V_m is the molar volume.

Thus, by combining the Eq. 47 to 55, the solute transfer procedure can be simplified as:

$$\frac{\partial c}{\partial t}+\nabla\bullet(Vc)=\nabla\left[D(\phi)\nabla c\right]+\nabla\left[D(\phi)h'(\phi)\left(c_{\mathrm{L}}-c_{\mathrm{S}}\right)\nabla\phi\right] \tag{58}$$

2.4 Temperature field method.

The governing equation for temperature T considering convection during solidification and dendritic growth can be written as:

$$\frac{\partial T}{\partial t}+\nabla\bullet\left(VT\right)=D_{\mathrm{T}}\nabla^{2}T+\frac{1}{2}\frac{L}{c_{p}}h'\left(\phi\right)\frac{\partial\phi}{\partial t} \tag{59}$$

$$S=\frac{1}{2}\frac{L}{c_{p}}h'\left(\phi\right)\frac{\partial\phi}{\partial t} \tag{60}$$

In present article, Lattice Boltzmann method (LBM) method has been used to solve heat transfer problem. According to the lattice Bhatnagar-Gross-Krook (LBGK) model, the distribution function of temperature $g_k(x,t)$ with a source item S can be given as:

$$g_{k}\left(x+\mathbf{e}_{k}\delta_{t},t+\delta_{t}\right)-g_{k}\left(x,t\right)=-\frac{1}{\tau_{\mathrm{T}}}\left[g_{k}\left(x,t\right)-g_{k}^{(eq)}\left(x,t\right)\right]+\delta_{t}w_{k}S \tag{61}$$

in which, x, t, e, δ_t and w represent lattice position, lattice time, time step, discrete lattice velocity vector, time step and weight coefficient, respectively. The subscribe k refers to discrete direction. τ_{T} is the relaxation time, which is associated with the thermal diffusivity D_T by:

$$D_{\mathrm{T}}=c_{\mathrm{s}}^{2}\delta_{t}\left(\tau_{\mathrm{T}}-0.5\right) \tag{62}$$

According to the Bhatnagar-Gross-Krook (BGK) collision operator, the density equilibrium distribution $g_{k}^{(eq)}(x,t)$ function is given as:

$$g_{k}^{(eq)}(x,t)=w_{k}T(x,t)\left[1+\frac{\mathbf{e}_{k}\bullet\mathbf{u}}{c_{s}^{2}}\right] \tag{63}$$

2.5 Evaluation indicators.

In present article, the characteristics of impacting-freezing seawater droplet are evaluated from the following two aspects: droplet dynamics and seawater freezing.

The spreading factor β and height factor H^* are the crucial indicators of droplet spreading.

$$\beta=\frac{D}{D_{0}} \tag{64}$$

$$H^{*}=\frac{H}{D_{0}} \tag{65}$$

in which, D_0 is the initial diameter of the seawater droplet, D stands for the contact width between the droplet and the low temperature surface, and H represents the distance between the top of droplet and the surface.

Freezing efficiency η reflects the ratio of the ice crystal area A_{seaice} to the droplet area $A_{droplet}$.

$$\eta = \frac{A_{seaice}}{A_{droplet}} \tag{66}$$

Besides, Peclet number is induced to describe the ratio of dendrites growth to salt diffusion, and it is expressed as:

$$Pe = \frac{U_{den} R_{den}}{2D_L} \tag{67}$$

where U_{den}, R_{den} and D_L stand for tip growth rate, tip radius and diffusion coefficient [25].

3. Numerical solutions

The coupling processes of seawater droplet impacting and freezing contain solid-liquid phase change, solute migration, temperature diffusion, and fluid flow, and there are complex interactions between them. Therefore, the numerical solutions are conducted by combining of multi-physical field coupling and multiscale simulation method, and the details will be described in this section.

3.1 Basic assumption

In present article, some key assumptions in the simulation are made as follows:

(1) The freezing point of seawater droplet is determined by the NaCl-H_2O phase equilibria diagram [8].

(2) The subcooling degree indicates the temperature difference between the seawater droplet and the triple point of pure water (0°C).

(3) The initial stage of seawater droplet is considered to be subcooled seawater with the subcooling degree.

(4) The heat convection between the air and the seawater droplet surface is neglected, and the temperature of the air is a constant value, which is set the same as the initial subcooling degree of the seawater droplet.

3.2 Model validation.

In order to ensure the accuracy of the mathematical model, the impacting model of water droplet at ambient temperature is verified firstly. Spreading Factor is a critical parameter used to characterize the dynamic spreading behavior of a droplet after impacting a solid surface. It quantifies the ability to spread outward post-impact and serves as a key quantitative indicator for evaluating dynamic wetting processes. According to Fig. 2A, by comparing the spreading factor during the impacting and

rebounding process with the experiment result from Ref. [50] and the simulated data from Ref. [51], it can be find that the MRT LBM model can well predicted the shape of impacting droplet and the kinetic parameter. When the droplet impacts on the solid wall, inertial forces drive rapid outward spreading of the droplet. After the droplet reaches its max diameter, it begins to retract under the action of surface tension. Subsequently, residual inertial forces combined with capillary forces from substrate wetting effects drive the re-expansion of the droplet edge outward. Meanwhile, from Fig. 2B, it can be seen that there is linear relationship between Δp and 1/R through Laplace test with γ equals to 0.5. Fig. 2C further verifies the reliability of the LBM model through grid independence verification. As shown in the figure, the spreading factor no longer exhibits significant variation with further increases in the computational grid density. To optimize computational efficiency, a grid size of $2560\Delta x \times 1280\Delta y$ is selected. Additionally, the mathematical model for the directional solidification process of subcooled seawater has been validated through the experiment data, and the experimental setup and procedure are described in Ref. [25, 26]. As shown in Fig. 2D, the tip growth rate during seawater directional freezing between the simulation and experimental data are both in the range of 0.5-2.5mm/s. Moreover, according to Fig. 2E, the morphological comparison of numerical simulation results with experimental observations of directional freezing of seawater and icing of brine droplets from Ref. [39] also demonstrates that the mathematical model can accurately predict the growth process of ice crystals within seawater droplet. It can be clearly seen from the images that there are dendritic differentiation structures with plenty of high-concentration brine pockets within the ice layer and salt channels between the dendrites. There is also a concentration diffusion layer at the top of the ice layer.

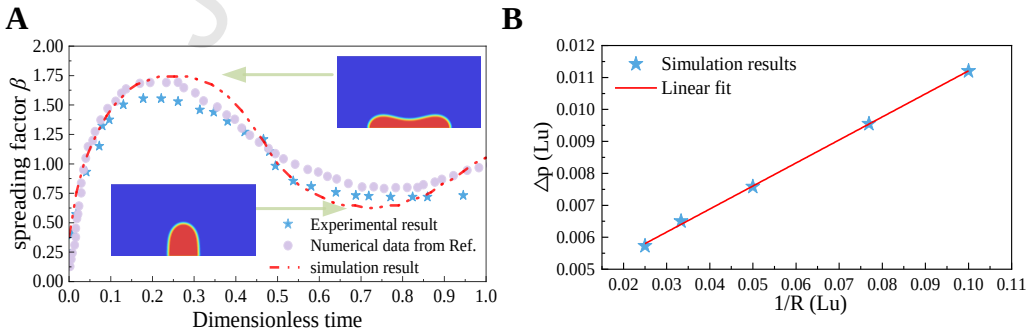

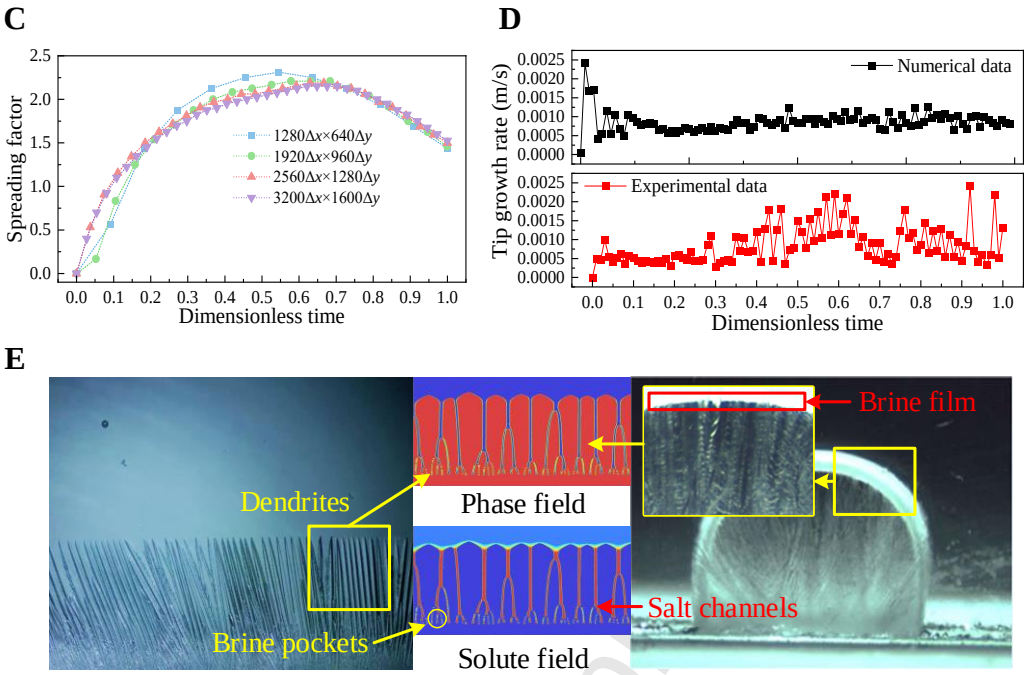

Fig. 2 Model validation. A. Numerical validation of the present MRT-LBM D2Q9 model against the experimental data from Ref. [50] and numerical data from Ref. [51]. B. Numerical validation of the Laplace's law based on the pressure difference across the interface. C. Verification of mesh independence based on droplet impacting on solid surface at ambient temperature. D. Comparison between the simulation and experimental data of the tip growth rate during seawater directional freezing. E. Morphological comparison of numerical simulation results with experimental observations of directional freezing of seawater and icing of brine droplets from Ref. [39].

3.3 Physical model and numerical details.

The physical model of the seawater droplet impacting and freezing coupling processes on low-temperature cold surface is illustrated in Fig. 1C. The computational domain is set as $2560\Delta x \times 1280\Delta y$, and the seawater droplet is set in the middle of the area with the initial diameter of $600\Delta x$. The initial seawater salinity and velocity are 0.030kg/kg and 5mm/s. Moreover, considering the actual freezing processes, such as the spray icing on marine vessels and offshore structures [52], the initial temperatures of seawater is considered to be the same as the low-temperature surface, and the subcooling degree is set as 15°C. Therefore, the droplet will nucleate and freeze immediately at the solid-liquid-gas three-phase interface after impacting on the cold surface, and there is no heat transfer process caused by the temperature difference between the droplet and the low temperature surface at

the initial stage. Besides, the other physical parameters are listed in Table 1.

Both the boundary of phase field and solute field are set as zero Neumann boundary condition. The temperature boundary condition of the droplet surface is set as Dirichlet boundary condition with a constant temperature. Meanwhile, the hydrodynamic boundary is set as non-equilibrium bounce-back scheme.

Table 1 Physical parameters of the impacting and freezing seawater droplet.

Parameters	Unit	Value
Anisotropy constant ε_{xy} [53]	-	0.02
Mesh size	-	2560×1280
Melting temperature, T_m	K	273.15
Solute diffusion coefficient of solid phase, D_S [54]	m^2/s	2.56×10^{-11}
Solute diffusion coefficient of liquid phase, D_L [54]	m^2/s	5.68×10^{-10}
Grid spacing, $\triangle x,\triangle,y$	m	1×10^{-7}
Interface thickness, λ	m	2×10^{-7}
Interface energy, σ	J/m^2	0.0758
Equilibrium partition coefficient, k^e	-	0.075

3.4 Solving framework.

As shown in Fig. 3, the multi-physical field coupling method is conducted to obtain the phase field, concentration field, temperature field and flow field parameters in the process of seawater droplet impacting and freezing. Firstly, the multi-component multi-relaxation time D2Q9 LBM method is applied to distinguish the gas-liquid phase interface and calculate the dynamic parameters. Moreover, the change of the solid-liquid phase interface and the mass transfer process are solved by the phase field theory and Fick's second law using the finite difference method. Besides, considering the larger time and space scale of the heat transfer process, the temperature field is adopt by single relaxation LBM method combing with multiscale simulation method. The physical fields coupling is achieved through parameter transfer, in which the phase field and the solute field are coupled by the phase field parameter ϕ and the solid and liquid concentration c_L and c_S, and the temperature field and the phase field are transferred by temperature T and ϕ. Meanwhile, with the solidification of seawater, the phase

field parameter ϕ acts on the droplet spreading in the form of solid boundary condition. The flow of the liquid phase in the unsolidified area will also react on the temperature field and solute field.

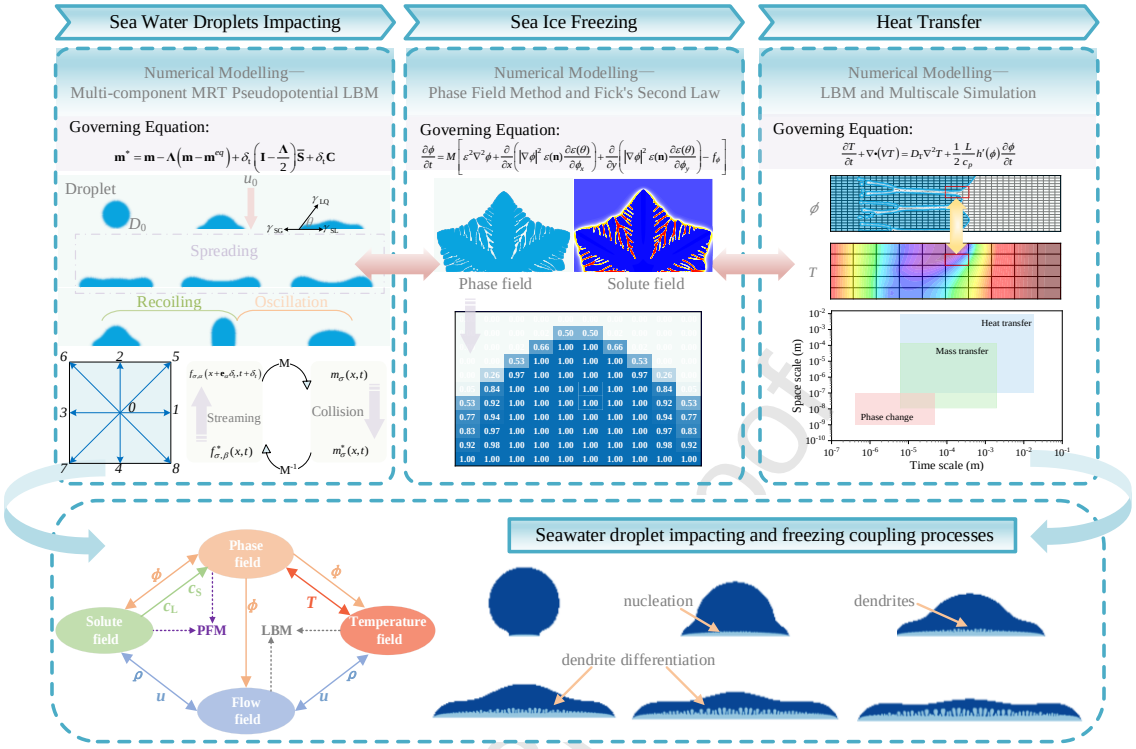

Fig. 3 The framework of multi-physics field joint solution and parameter transfer mechanism.

4. Results and discussion

In this section, the impacting and freezing coupling processes of seawater droplet on cold surface are numerically studied. Firstly, the droplet morphology, internal concentration, temperature and flow field distribution during the droplet impact process are analyzed. Additionally, the effects of surface wettability, impacting velocity, surface temperature and seawater salinity on dynamic and phase change behaviors including the spreading factor and the freezing efficiency are explored, and the variable range of the operating parameters are shown in Table 2.

Table 2 Variable range of the operating parameters.

Parameters	Value
Contact angle θ (°)	60, 90, 120, 150
Impacting velocity u_0 (mm/s)	-3, -5, -7, -9
surface temperature T_0 (K)	253.15, 255.65, 258.15, 260.65, 263.15

Seawater salinity x_0 (kg/kg)	0.025, 0.030, 0.035, 0.040

4.1 Droplet impact dynamics and freezing morphologies.

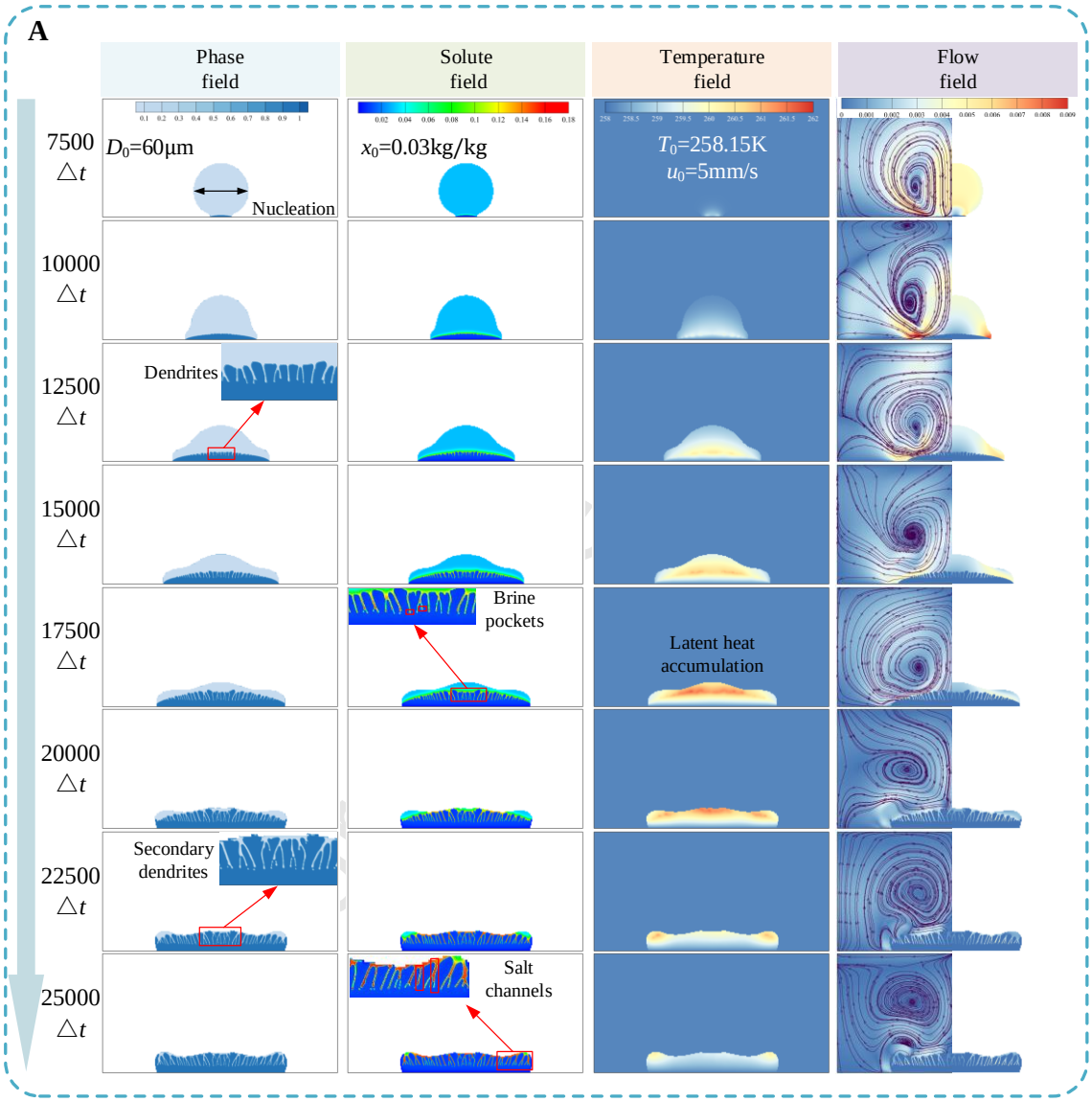

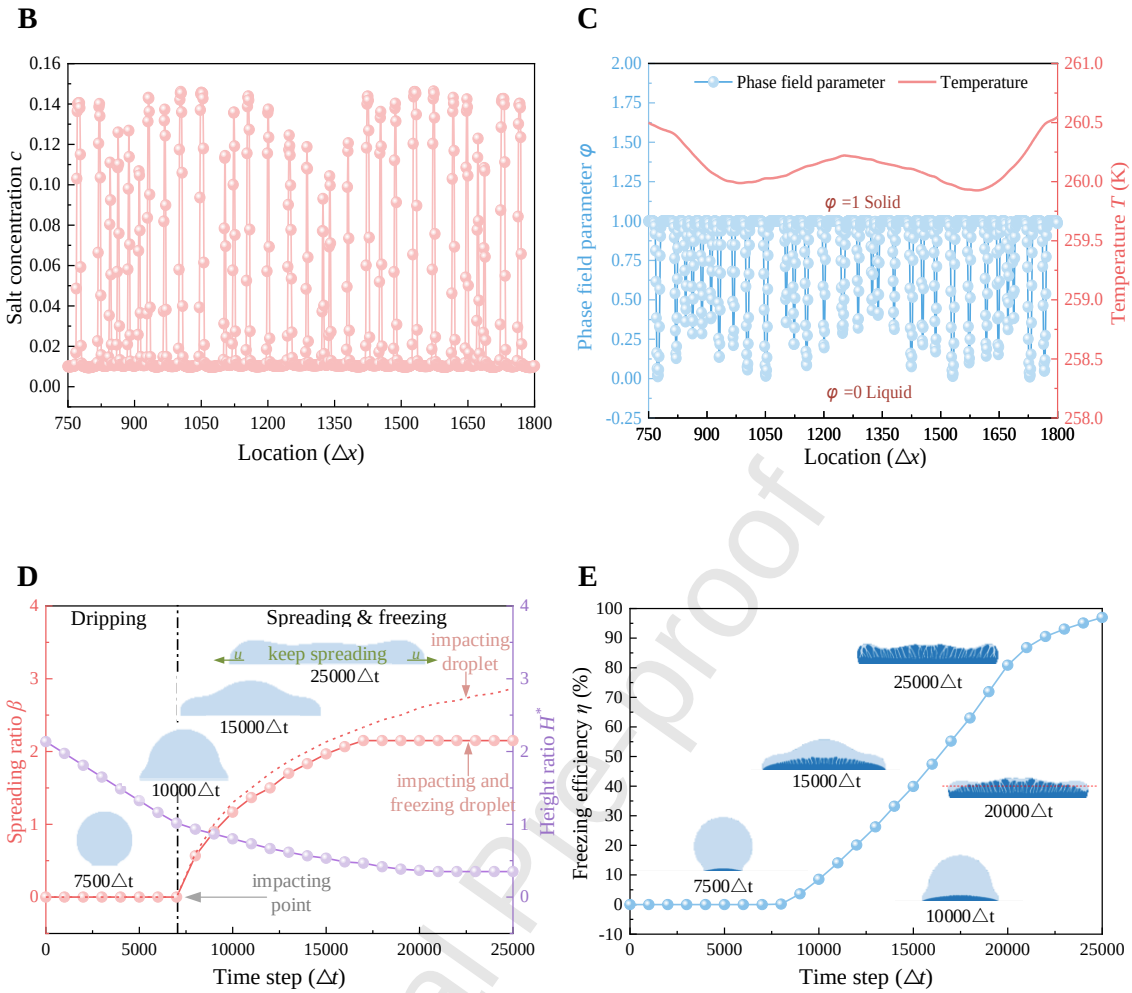

Fig. 4 Characteristics of impacting-freezing seawater droplet. A. Schematic diagram of an impacting seawater droplet on cold surface. B. The salt concentration in simulation on 110Δy at 20000Δt. C. The phase field parameter and temperature in simulation on 100Δy at 20000Δt. D. The evolution of spreading ratio β and height ratio H^* with varying time. E. Time evolution of freezing efficiency η.

Fig. 4 illustrates the characteristics of a seawater droplet impacting and freezing on the cold surface from the aspects of phase field, solute field, temperature field and flow field. The freezing temperature is set as -15°C with the contact angle of 90°, and the impacting velocity of the seawater droplet is 5mm/s. According to Fig. 4A, when the time step reaches 7500Δt, the seawater droplet comes into contact with the low-temperature surface and nucleates at the bottom surface. Initially, based on the phase field at 10000Δt, after the seawater droplet impact on the cold surface, it spreads horizontally. As the contact area between the droplet and the cold surface increases, the freezing process starts, forming

a morphology characterized by high centers and low sides. As time passes from 12500Δt to 20000Δt, the continuous spreading and freezing of the droplet causes the solid-liquid-gas three-phase contact line to extend. During crystallization, ice layer grows from the bottom towards the top, leading to dendritic differentiation caused by competitive growth among the ice crystals. Ultimately, during 20000Δt to 25000Δt, the droplet stop spreading and the sea ice continues to grow upwards. The frozen seawater droplet shows a central-concave pattern, and there is a thin high concentration brine film between the top dendrites and the gas-liquid interface.

Unlike pure water, the freezing of a seawater droplet is complicated by salt migration. In the early solidification stages, salt is expelled from the solution, forming a diffusion layer on the ice surface. The accumulation of salt significantly impacts ice crystal growth. As shown in the solute field at 17500Δt, there are plenty of high concentration areas within the ice layer, named brine pockets. The reason is as follows, during the ice crystals growth, dendrites formed as a result of the existence of anisotropy, and the solute at the root of the dendrites cannot diffuse in time. As dendrites merge, part of the salt water becomes trapped within the ice layer. According to the concentration distribution along the horizontal direction on 110Δ*y* in Fig. 4B, it is revealed that due to the presence of salt cells, the max salt concentration of brine pockets is approximately 0.15 kg/kg.

The solidification of the seawater droplet is also accompanied by the release of latent heat, which plays a critical role in influencing the temperature within the seawater droplet. The variation of temperature field under different time step reveal that with the increase of sea ice area, the temperature inside the droplet increases gradually. From 10000Δt to 17500Δt, the max temperature of droplet increases from 259.92K to 261.48K. In the early stage of icing, only the temperature near the phase transition zone increases. However, as the ice layer continues to grow, and the freezing efficiency increases, leading to the freezing heat continues to accumulate. Meanwhile, from the phase field parameter and temperature on 100Δy at 20000Δt shown in Fig. 4C, it can be seen that the maximum temperature difference at the section is 0.65 K. From the distribution of phase field parameter, it can be seen that there are solidified dendrites on both sides of the droplet, and the latent heat causes its temperature to rise. The temperature in the middle of the droplet is also relatively high. Although the dendrite differentiation in this area has been completed, the solidification heat at the top will prevent its temperature from dropping rapidly. In addition, due to the heat conduction from the low-temperature surface, the temperature of other solidified areas begins to decrease.

Additionally, the impacting seawater droplet also undergoes change in kinetic energy, and drives the flow of surrounding air. From the perspective of flow velocity in 10000Δt, the droplet is still in the spreading stage, and the flow velocity within the droplet reaches its peak along the edges of the frozen area. Meanwhile, vortexes are generated at the interface boundary between the air and the droplet above. However, as time goes by, the fluid velocity in the flow field gradually decreases, indicating that the influence of the dynamic parameters on droplet spreading gradually decreases.

The complex interactions of phase changes, solute migration, temperature variations, and fluid dynamics during the impacting and freezing of seawater droplets contribute to unique freezing behaviors and structures. Fig. 4 D and E present the variation of spreading ratio β, height ratio H^* and freezing efficiency η throughout the processes of seawater droplet dripping, nucleation and freezing. After reaching the impacting point, the freezing rate begins to rise, indicating that the seawater droplet is transitioning from dripping to the freezing, and is also accompanied by a rise in β and a decline of H^*. Compared with droplet impacting without freezing, the formation of ice layer at the droplet bottom effectively restricts its further spreading, and by the time step reaches 17500Δt, the spreading factor stabilizes. However, the central portion of the droplet continues to widen, which leads to the decrease of height ratio. In the final stages of freezing, the accumulation of salt within the liquid phase significantly reduces the freezing rate and the height ratio no longer changes.

4.2 Effect of surface wettability on droplet impact and freezing processes.

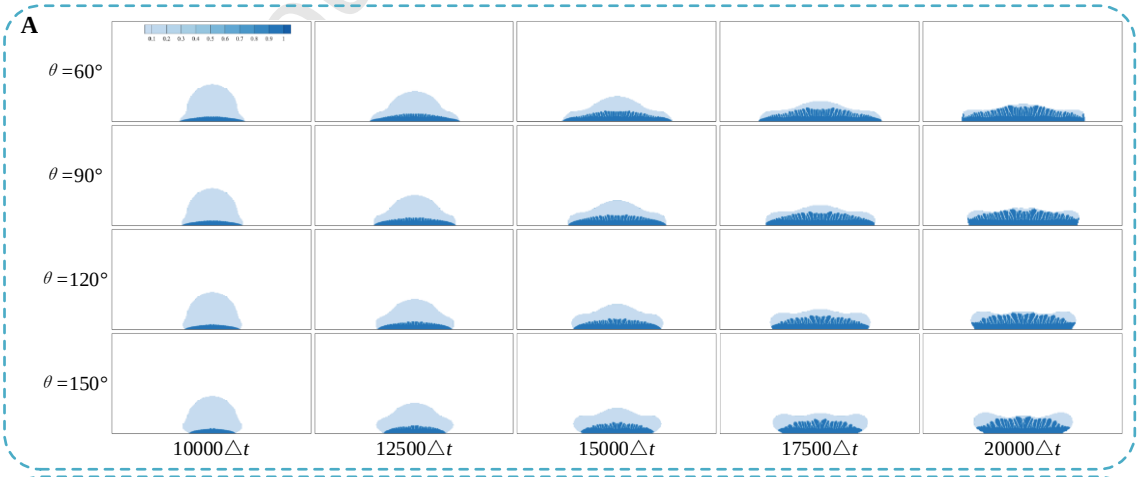

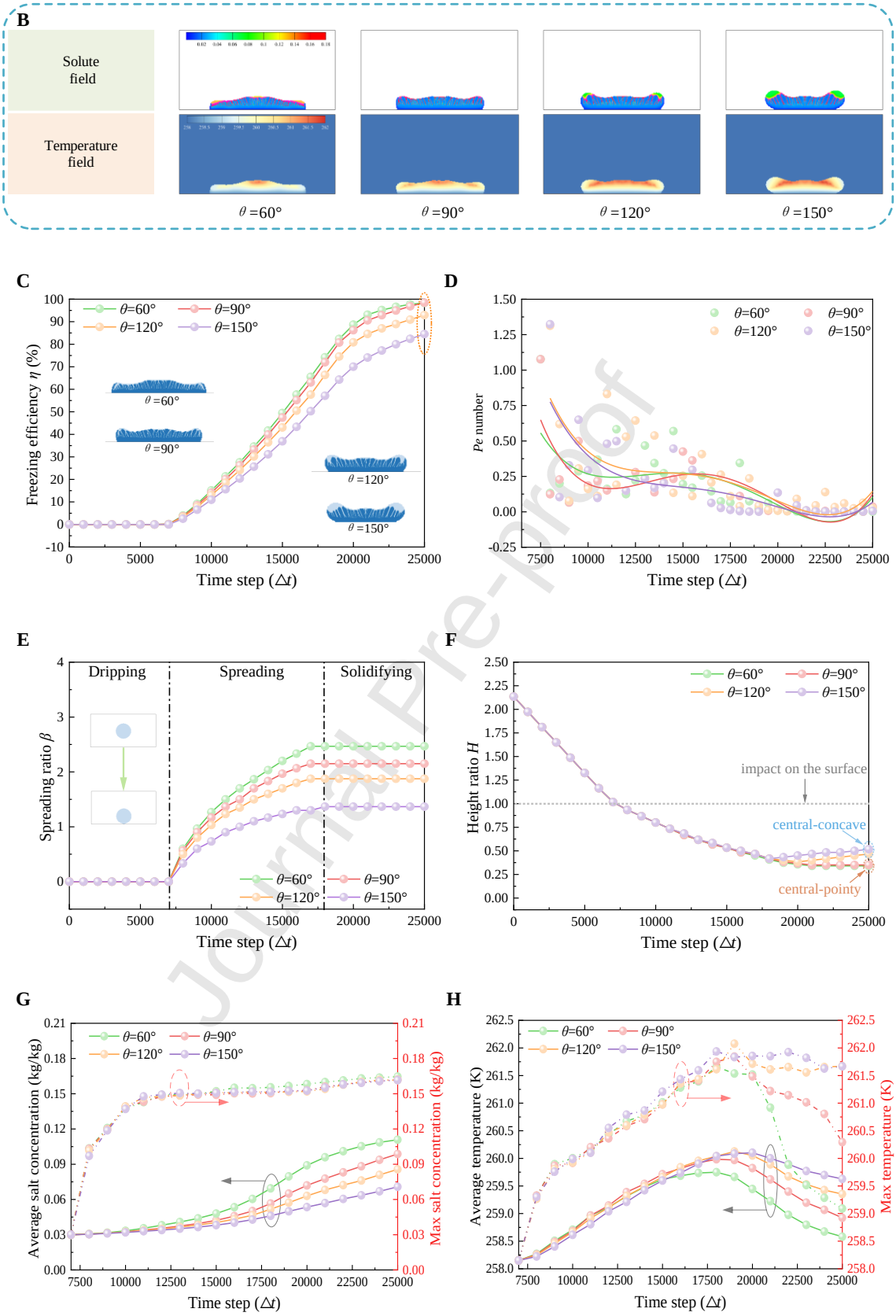

Fig.5 Characteristics of impacting-freezing seawater droplet under different contact angle θ. A.

Temporal evolutions of impacting-freezing droplet parameters under different contact angle θ. B. Simulation results of the solute field and temperature field at 20000Δt. C. The change of freezing efficiency η with time. D. Time evolution of *Pe* number with contact angle θ. E. The evolution of spreading ratio β with varying time. F. The evolution of height ratio *H* with varying time. G. Evolutions of average and maximum salt concentration. H. Evolutions of average and maximum droplet temperature.

The characteristics of impacting-freezing seawater droplet under different contact angle θ are displayed in Fig. 5. The temporal evolution of the phase field parameters depicted in Fig. 5A indicates a significant transformation in the freezing pattern of the droplet as the contact angle increases, transitioning from a central-pointy to a central-concave structure. During the initial 10000 time steps, the influence of the droplet spreading on ice crystal formation is minimal, and the sea ice remains characterized by higher center and lower sides. However, as time goes by, the effect of droplet wettability on the sea ice morphology becomes increasingly pronounced. As θ increases, the surface wettability shifts from hydrophilic to hydrophobic. The wettability has a great influence on the flow process of the seawater droplet. For hydrophilic surfaces, the adhesion force between the droplet and the surface is large, and the inertial forces are used to overcome the adhesion forces and fluid-solid interaction forces accompanying the icing. As the droplet continues to spread, new nucleation points continue to appear at the bottom. The morphology of the completely frozen droplet is a structure with a high center and low sides. For hydrophobic surfaces, its hydrophobic properties prevent the droplet from continuing to spread horizontally, but the inertial forces will cause its center to move downward. This will cause the concave area in the center of the droplet to freeze completely first, and the sides to freeze later.

According to the relationship between freezing efficiency η and contact angle θ (shown in Fig. 5C), it indicates that as θ increases, the freezing efficiency diminishes at a consistent time step. When the time step is 25000$\triangle t$, the values of η at θ=60° and 150° are 98.35% and 84.48%, respectively. This indicates that the decrease in θ will promote the solidification of seawater. This is because, when the contact angle is very small, it is easier for the seawater droplet to form nuclei after contacting the low-temperature surface. The increase in the number of crystal nuclei will promote the solid-liquid phase change process and increase the freezing efficiency. However, as shown in Fig. 5D, there is no apparently difference in the average value of *Pe* number during freezing process. This is because the *Pe*

number measures the ratio of the phase change rate and mass transfer rate at the dendrite tip. When the contact angle increases, since the initial salinity and temperature of the droplet are the same, the phase change and mass transfer process at the solid-liquid interface will not change greatly due to the increase in nucleation points.

Furthermore, from Fig. 5E, when the contact angle arises from 60° to 150°, the max spreading factor drops from 2.47 to 1.37. The reduction of spreading ratio will lead to a decrease in nucleation area, subsequently delaying the evolution of ice layer. A smaller contact angle results in a larger spreading area, and the height on both sides of the droplet is very low, which is consistent with the shape of the ice layer at early stage. Thus, when the ice layer grows to the height of the droplet, it will present a central-pointy freezing pattern. Conversely, the droplet will present a structure with a concave center and protruding sides under the action of inertial force at large contact angle. When the center of the ice crystal grows to the concave part of the droplet, there is still unsolidified seawater on the left and right sides. Therefore, when the seawater is completely frozen, it will present a central-concave structure. It is worth noting that the freezing mode can also be judged by the change of the height coefficient H^*. As can be seen in Fig. 5F, due to the decrease of the center height of the droplet, the H^* continues to decrease in the freezing pattern with central-pointy. However, when the freezing mode changes to central-concave, the height of the two sides of the droplet exceeds the middle, and thus the height coefficient increases after falling to the bottom.

Besides, according to Fig. 5B and G, it can be seen that when the time step is 20000 $\triangle t$, the salt concentration of the liquid phase inside the droplet is higher owing to the higher freezing efficiency at low contact angle. Moreover, from the variation of average and max concentration during freezing time, it can be concluded that the changing trends are the same as that of freezing efficiency. When θ is 60° and 150°, the max concentration inside the droplet could reach 0.165kg/kg and 0.161kg/kg, respectively. This is because the morphology of droplet at small contact angle is flatter, and the limited diffusion area will also aggravate the enrichment of solutes.

From Fig. 5B, a significant high-temperature region can also be observed at the solid-liquid interface, resulting from continuous solidification. The temporal evolution of maximum and average temperatures within the seawater droplet shows an intriguing trend: although the freezing rate of ice formation is faster for smaller contact angles, the average internal temperature remains lower. Specifically, the maximum temperatures for contact angles of 60° and 150° are recorded at 259.09 K

and 261.67K, respectively. The underlying reason is that when the droplet fully contacts the low-temperature surface at smaller θ, the latent heat of phase change can also be quickly conducted. Meanwhile, the decrease of droplet temperature will promote the growth of ice crystals. Therefore, in the field of anti-icing engineering, hydrophobic materials with large contact angle are mainly developed to delay the growth of ice layer.

4.3 Effect of impacting velocity on droplet impact and freezing processes.

Fig. 6 depicts the characteristics of impacting-freezing seawater droplet under different impacting velocity u_0. The temporal phase field parameters provided in Fig. 6A indicates that higher-speed droplets initiate nucleation and dendrite growth earlier in the freezing process. As plotted in Fig. 6C, droplets with initial velocities between -5 mm/s and -9 mm/s are nearly completely frozen after a freezing time of 25000Δt. In contrast, the droplet with an initial velocity of -3 mm/s achieves only a 74.63% freezing efficiency. This is because the high-speed droplet still has high kinetic energy after impacting on the cold surface. The internal flow is conducive to the rapid removal of solidification heat to prevent the internal temperature of the droplet from continuing to rise and reduce the subcooling degree. Besides, under the inertial force, the droplet with higher u_0 contacts the low-temperature surface faster and gradually deforms with the contact line spreading. The arising initial speed will enlarge the impacting kinetic energy of the seawater droplet, and thus the spreading diameter goes up. The increase in spreading area helps to increase the number of crystal nuclei on the bottom of the droplet, thereby improving the freezing efficiency. As shown in Fig. 6E and F, when the initial velocity u_0 changes from -3mm/s to -9mm/s, the max spreading ratio rises from 1.73 to 2.90, and the min height ratio drops from 0.52 to 0.28. Consequently, the combination of earlier freezing and larger spreading factor contribute to the faster freezing rates in high-speed droplet. Moreover, because the profiles of freezing droplet are greatly determined by the limit of the icing range, the morphology of high-speed droplet tends to be central-pointy with two peaks on both sides, and with the decrease of u_0, the peaks disappear gradually. Besides, from the morphology of dendrites, it can be seen that high-speed droplet has more internal dendrites after freezing, and there is obvious competition for growth between each dendrites, resulting in a relatively smaller tip radius. From the variation of *Pe* number shown in Fig. 6D, the reduction of tip radius leads to a decrease in the average *Pe* number at higher impacting velocity.

Fig. 6B presents the internal salinity distribution of the seawater droplet after 25000 steps. The

droplet with an initial velocity of -9 mm/s has completely solidified, showing no further changes in salinity, while the droplet with an initial velocity of -3 mm/s remains in the freezing stage with a concentration gradient. From Fig. 6G, it is evident that as droplet velocity increases, both the average and maximum concentrations within the droplet rise slightly. As u_0 changes from -3 mm/s to -9 mm/s, the max salt concentration rises from 0.151kg/kg to 0.167kg/kg, which increases by 10.60%. This phenomenon occurs for two main reasons. Firstly, the increase in freezing rate aggravates the enrichment of solutes, preventing the salt discharged from solidification to diffuse in time. Secondly, the increase in u_0 makes the droplet morphology present a concave structure with wide sides, which limits the available space for upward solute diffusion. When the initial velocity of the seawater droplet increases, it will continue to spread on both sides under the action of inertia force. This phenomenon results in a large aspect ratio of the droplet, and the droplet becomes very thin. As the droplet impacts on the surface to form nuclei and freeze, salt continues to precipitate from the solid phase. However, since the liquid phase layer is very thin, the continuously precipitated salt lacks sufficient diffusion space. As the concentration gradient at the solid-liquid interface increases, high concentrations of solute will be enriched.

Observing the temperature distribution in Fig. 6B, the droplet with a higher initial velocity (-9 mm/s) has completely frozen and thus no longer generates solidification heat internally, and the temperature is closely approach to the cold surface. In contrast, the low-speed droplet remains in the solidification stage, accumulating significant latent heat at the solid-liquid interface. Additionally, as plotted in Fig. 6G, compared with the high-speed droplet, the average temperature and maximum temperature inside the low-speed droplet shows an increasing trend. As the impacting velocity u_0 increases from 3mm/s to 9mm/s, the max temperature of droplet decreases from 262.18K to 261.12K. The decline is attributed to the reduced contact area with the low-temperature surface at lower velocities, hindering effective heat diffusion. In addition, the decrease of freezing rate makes the icing time longer, and the continuous heat generation will also maintain the higher internal temperature. The velocity diagram in Fig. 6B also adds an important dimension to the analysis. After the high-speed droplet impacts on the cold surface and freezes, it is evident that there is still significant airflow velocity above its surface due to inertia. In contrast, the area above the low-speed droplet shows the presence of vortex, and the spreading of droplet is also basically stopped.

From the above research, it can be seen that the increase in initial velocity will accelerate the

freezing process of seawater droplet. Not only the thickness of the ice layer is very thin, but the large contact area will also cause the latent heat of solidification to diffuse rapidly to the low-temperature surface, which is extremely unfavorable for anti-icing. However, in the actual process, the impact speed of droplet is difficult to control. Hot gas anti-icing technology can use high-temperature gas to heat droplet to prevent freezing. At the same time, it can also reduce the impact speed of droplets by applying the airflow in the opposite direction of the droplet movement, thereby delaying freezing, and using high-temperature gas heating to melt ice quickly.

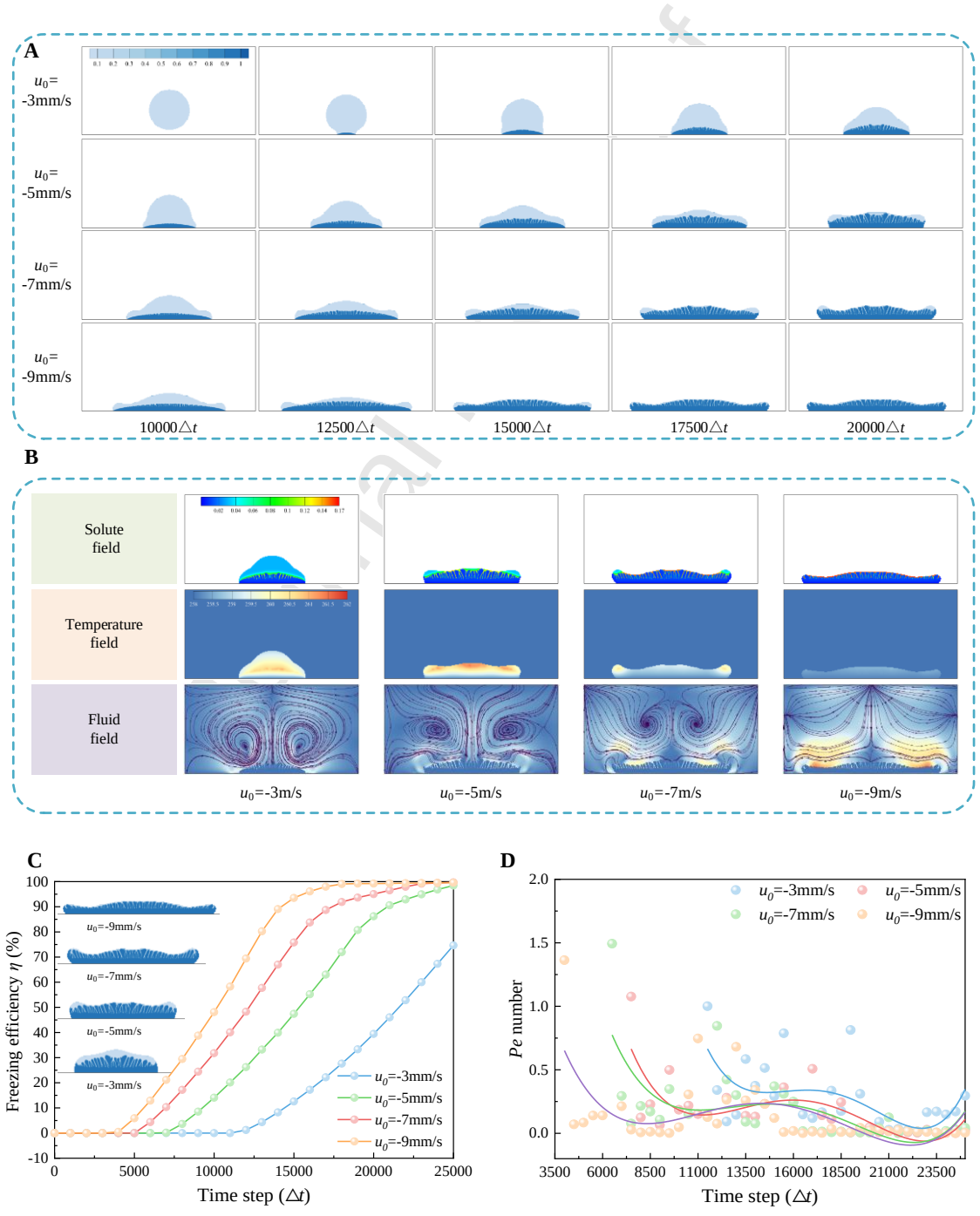

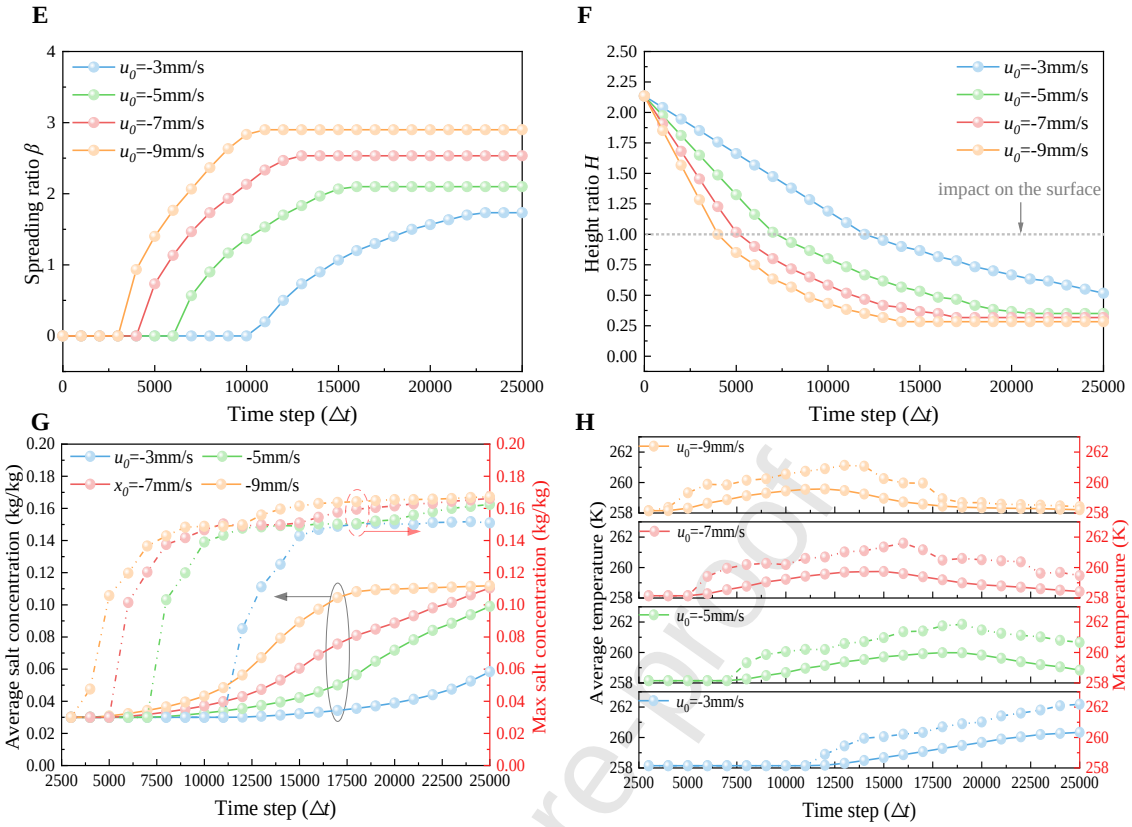

Fig. 6 Characteristics of impacting-freezing seawater droplet under different impacting velocity u_0. A. Temporal evolutions of impacting-freezing droplet parameters under different initial speed u_0. B. Simulation results of the solute field, temperature field and fluid field at 25000Δt. C. The change of freezing efficiency η with time. D. Time evolution of Pe number with contact angle θ. E. The evolution of spreading ratio β with varying time. F. The evolution of height ratio H with varying time. G. Evolutions of average and maximum salt concentration. H. Evolutions of average and maximum droplet temperature.

4.4 Effect of surface temperature on droplet impact and freezing processes.

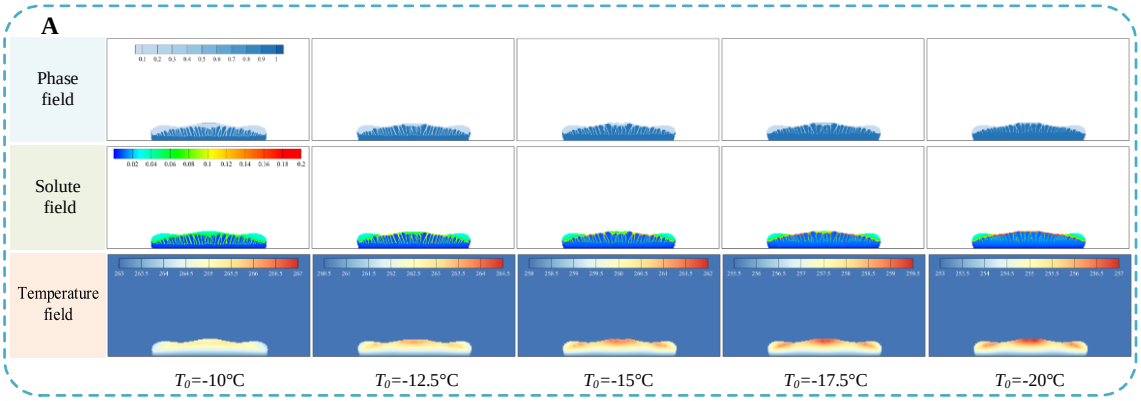

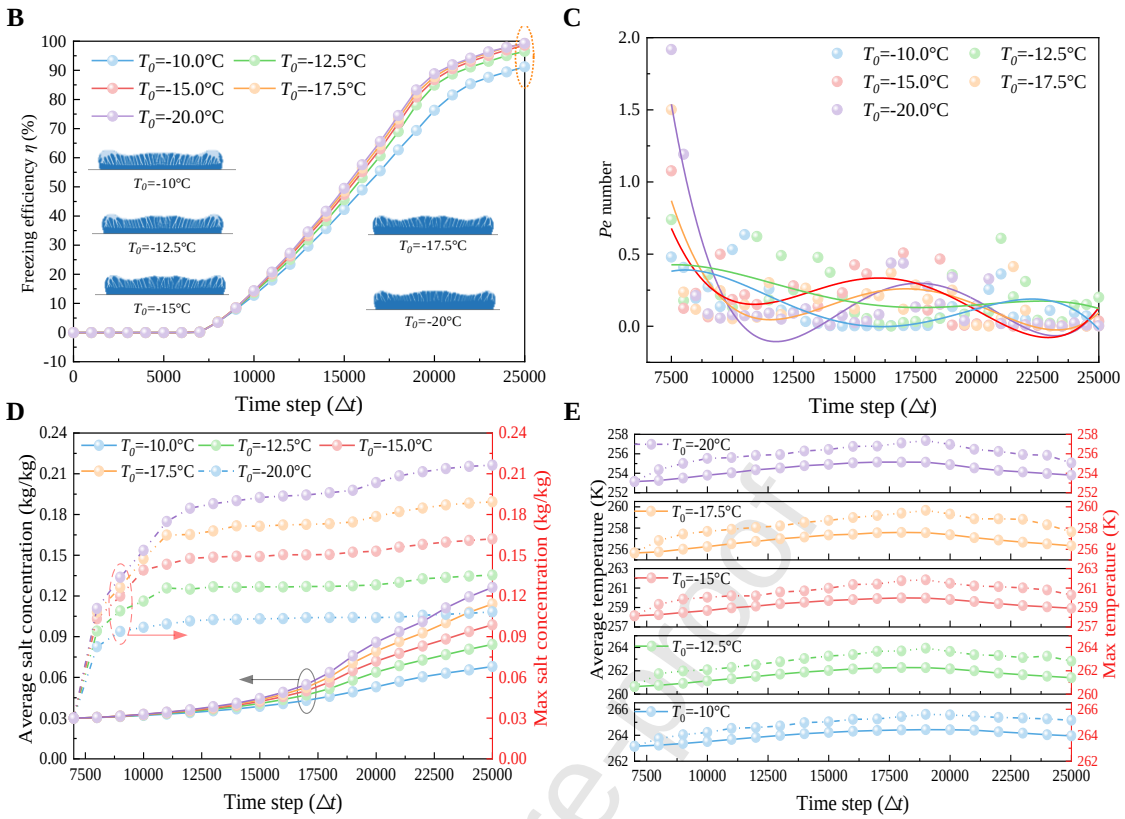

Fig. 7 Characteristics of impacting-freezing seawater droplet under different surface temperature T_0. A. Simulation results of the phase field, solute field and temperature field at 20000Δt. B. The evolution of freezing efficiency η with varying time. C. Time evolution of *Pe* number with different x_0. D. Evolutions of average and maximum salt concentration. E. Evolutions of average and maximum droplet temperature.

Fig. 7 illustrates the characteristics of impacting-freezing seawater droplet under different surface temperature T_0. The subcooling degree serves as the driven force of seawater solidification, and thus T_0 significantly affects the morphology of freezing droplet when other dynamic parameters remain consistent. Analysis of the phase field parameter in Fig. 7A reveals that at a time step of 20000Δt, the ice layer formed at T_0=-10°C is notably thinner than that at T_0=-10°C. Additionally, distinct dendritic differentiation is more apparent in the lower temperature condition. Meanwhile, from the time-evolution of freezing efficiency η shown in Fig. 7B, both the freezing efficiency η and phase change rate increase with the drop of T_0. By the time the time step reaches 25000Δt, the values of η at -10°C and -20°C are 91.22% and 99.25%, respectively. The increase in subcooling degree directly

enhances the growth rate of dendrites. This is accompanied by a thicker dendritic structure at lower temperature, which facilitates the formation of a denser ice layer. The relationship between subcooling degree and dendrites behavior is further supported by the changes in the Peclet number shown in Fig. 7C. As the surface temperature decreases from -10°C to -20°C, the average *Pe* number increases from 0.14 to 0.18. The increase is attributed to the higher growth rate and radius of dendrites, resulting in a higher *Pe* number during seawater droplet freezing.

The solute analysis at 20000Δt presented in Fig. 7A, along with the variation in max and average salt concentrations shown in Fig. 7D, highlights the significant impact of T_0 on solute transport during the droplet freezing. As T_0 descends from -10°C to -20°C, the max concentration of solute filed at 25000△t rises from 0.108kg/kg to 0.216kg/kg, which increases by 1 times. The increase can be attributed to the greater disparity between the phase change rate of ice crystals and the diffusion rate of solutes as T_0 decreases. Consequently, more salt becomes trapped within the sea ice, combing with the max concentration in the solution grows up.

According to the temperature field of freezing droplet depicted in Fig .7A, with decreasing T_0, the area of high temperature within the droplet expand at the same time step. The data in Fig. 7E illustrates that as T_0 decreases from -10°C to -20°C, the max temperature rise inside the droplet relative to T_0 increases from 2.46K to 4.21K. This phenomenon occurs primarily because, as the degree of subcooling increases, the phase change rate accelerates and the solidification heat generated during the freezing process cannot dissipate quickly enough. Therefore, the temperature gradient inside the droplet will increase, and the heat will be concentrated in the solid-liquid interface area. The rise in temperature will cause a decrease in subcooling degree, thereby reducing the growth rate at dendrite tips. When the latent heat released per unit time decreases, the solid-liquid interface temperature begins to decrease, the subcooling degree increases, and the dendrite growth rate accelerates again. This phenomenon can also be confirmed by the changes in the *Pe* number and dendrite morphology. The *Pe* number will first decrease, then increase, and then decrease during the freezing process, and the lower T_0, the more obvious this change is. When the subcooling degree is large, the solid ice layer of the seawater droplet is thicker, but as the internal temperature gradient increases, the instability of the solid-liquid interface increases, and the dendrites begin to differentiate. However, despite the increase in temperature, the subcooling degree is still large, resulting in significant dendrite coarsening.

4.5 Effect of seawater salinity on droplet impact and freezing processes.

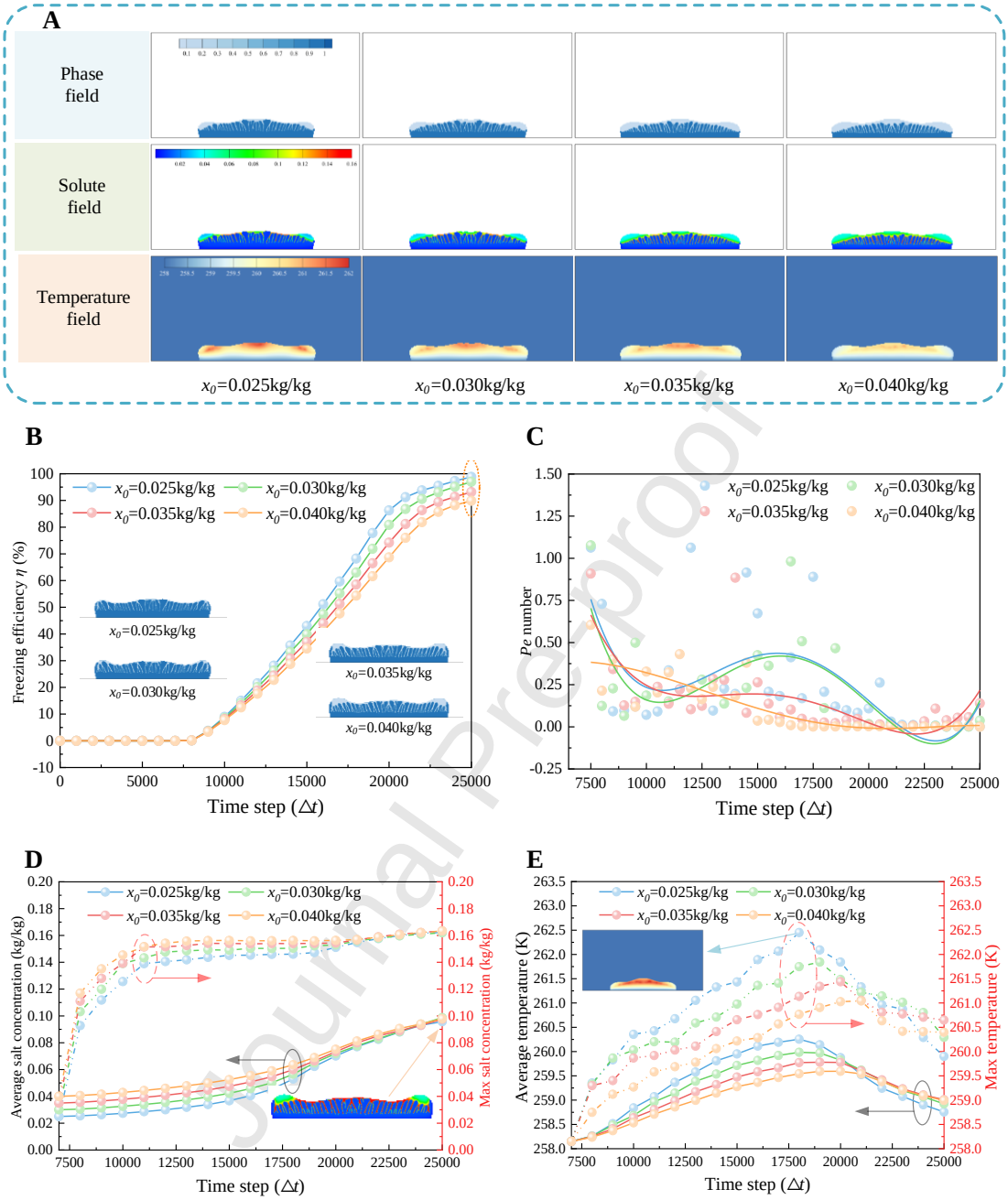

Fig. 8 Characteristics of impacting-freezing seawater droplet under different initial salinity x_0. A. Simulation results of the phase field, solute field and temperature field at 20000Δt. B. The evolution of freezing efficiency η with varying time. C. Time evolution of *Pe* number with different x_0. D. Evolutions of average and maximum salt concentration. E. Evolutions of average and maximum droplet temperature.

Although the salinity of seawater droplets has little effect on droplet dynamics, it will have a

significant impact on the heat and mass transfer during the freezing process. Hence, the characteristic of impacting-freezing seawater droplet under different initial salinity c is outlined in Fig. 8. According to Fig. 8A and B, it is obvious that the freezing rate of seawater droplets decreases with increasing x_0, and the difference in freezing efficiency η becomes more pronounced as freezing time progresses. When freezing time is 25000Δt, the freezing efficiency at 0.025 kg/kg and 0.040 kg/kg are 98.83% and 89.67%, respectively. Additionally, the phase field parameter reveals that ice dendrites form higher and coarser structures at lower x_0 with several secondary dendrites appearing. This is because the inhibition of solute enrichment on ice crystal growth will be relieved when the salt concentration decreases. At the time, the disturbance at the solid-liquid interface is not easily amplified, and the phase interface is more stable. According to Fig. 8C, the increase of initial concentration will cause the decrease of Pe number, which further proves that the difference between the phase transition rate and diffusion rate plays a dominant role in seawater freezing process. The reason behind this is that higher initial concentration will lower the freezing point, and thus the dendrite growth rate will decrease with the reducing subcooling degree.

The solute distribution observed during the crystal growth process suggests that at higher x_0, there are numerous regions of high salt concentration between the dendrites due to the downward movement of the solidus line. Solute redistribution during solidification is an important process for seawater freezing. The salt concentration in the solid phase is lower than the initial concentration, and the diffusion rate of the solute in the liquid phase is also lower than the growth rate of the dendrite. The solute precipitated by solidification cannot fully diffuse into the liquid phase and will be enriched at the front of the dendrite. The increase of liquid concentration will increase the concentration gradient at the solid-liquid interface. When the solute concentration in the solid phase is low and the solute concentration on the interface is high, it is difficult for the solute to diffuse into the liquid phase. Fig. 8D provides the average and max salt concentration inside the seawater droplet, it can be concluded that in the early stage of freezing, due to the difference in initial concentration, the average and maximum concentration of high-concentration seawater droplet are higher than those of low-concentration droplet. However, with the evolution of the ice layer and the enrichment of salt, the average and maximum concentrations of low initial salinity droplets gradually increase. Although the initial concentrations are different, higher x_0 will leads to the slower freezing rate. At the same time step, there are a large number of unfreezing areas. Therefore, the average concentrations in the later

stage are similar. Besides, from the solute field of seawater droplet of x_0=0.04kg/kg at 25000Δt, it can be seen that the high concentration of salt is mainly distributed inside the dendrites, that is the brine pockets. However, the high concentration area of the low-concentration brine droplets is located in the unfrozen region.

The effects of different x_0 on the temperature profile are investigated in Fig. 8E. The results reveal that with the increasing x_0, both the average and maximum temperature within the droplet decrease. As x_0 ascends from 0.025kg/kg to 0.04kg/kg, the peak max temperature descends from 262.45K to 261.04K. The latent heat released during solidification raises the temperature at the solid-liquid interface, affecting its stability. Consequently, the decrease in temperature further supports the conclusion that higher salinity inhibits the freezing process. Additionally, the longer freezing duration of high-salinity droplet allows for a more extended temperature rise, resulting in higher average temperatures in the later stage.

From the above research results, it can be clearly seen that the increase in salinity has a great impact on the phase change and freezing process of seawater droplet. The increase in salt concentration will significantly reduce the ice formation rate. Therefore, in the anti-icing of marine structures, it is possible to consider spraying high-concentration salt water on the surface or adding an appropriate amount of salts to the anti-icing coating on the surface of the structure to achieve the purpose of inhibiting ice formation. Additionally, in the field of seawater freezing desalination, due to the existence of brine pockets, the primary desalination rate is low, and the higher salt concentration, the lower freezing efficiency and desalting rate will be (shown in Fig. 8). This also confirms that multi-stage freezing desalination is a necessary choice for developing seawater desalination technology to improve desalination efficiency.

5. Conclusions

In present article, a combined phase-field and multi-relaxation-time lattice Boltzmann method model is established to simulate the seawater droplet impacting and freezing coupling processes. By using the developed novel method, the coupling effect between the seawater droplet fluid dynamics and solidification is achieved, and the interface variation of solid-liquid-gas phases can be easily tracked and accurately described. Meanwhile, considering the ion migration and phase interface fluctuation in the process of seawater freezing, the temperature and salinity distribution inside the droplets can also

be obtained. Through the numerically studies, the characteristics of impacting-freezing seawater droplet are investigated, and the influences of surface wettability, impacting velocity, surface temperature and initial salinity on freezing efficiency and dynamic behavior are discussed. The conclusions obtained are drawn as follows:

(1) Compared to the droplet impacting behavior at ambient temperature, there is no rebounding effect after seawater droplet impacting on the cold surface owing to the sea ice solidification. The spreading factor remains unchanged after reaching its peak value. The morphology of frozen seawater droplet is greatly influenced by the dynamic parameters and thermodynamic parameters. There is a significant dendritic differentiation phenomenon at the solid-liquid interface combining with a high-concentration brine film above the dendrites. High concentrations brine pockets also exhibit in the ice layer owing to the differences in phase change and mass transfer rates.

(2) With the increase of contact angle, the morphology of ice crystals changes from central-pointy to central-concave. Smaller contact angle is conductive to the growth of sea ice, and reducing surface wettability is beneficial for anti-icing. When the time step is 25000$\triangle t$, the freezing efficiency at θ=60° and 150° are 98.35% and 84.48%, respectively.

(3) The increase in impacting velocity will enhance the spreading factor and accelerate the freezing rate. Under the same operating conditions, when high-speed droplet with initial velocity of -9mm/s is completely solidify, the freezing rate of low-speed droplet with initial velocity of -3mm/s is only 74.63%.

(4) The surface temperature has little effect on the droplet dynamic parameters, but with the increase of subcooling degree, the growth rate of ice crystal increases slightly. At the same time, the dendrites change from sharp to round, and more salt solution enriched between the dendrites. When the surface temperature drops from -10°C to -20°C, the max concentration inside the droplet rises from 0.108kg/kg to 0.216kg/kg.

(5) An increase in initial salinity inhibits the growth of ice crystals, which helps to mitigate local latent heat accumulation and balance the differences between diffusion and phase change rates. Consequently, despite an increase in initial salinity, the maximum salt concentration inside the droplet does not rise significantly.

Acknowledgements

The authors acknowledge the financial support provided by National Natural Science Foundation of China (NO. 52476094, 52401352), Shandong Provincial Natural Science Foundation (ZR2023ME146).

References

[1] Y. Zhang, L. Zhang, G. Luo, Study on de-icing criterion of anti-icing coating and simulation analysis method of mechanical de-icing process for polar ship superstructure, Ocean Engineering, 288 (2023) 115811.

[2] A.R. Dehghani-Sanij, S.R. Dehghani, G.F. Naterer, Y.S. Muzychka, Marine icing phenomena on vessels and offshore structures: Prediction and analysis, Ocean Engineering, 143 (2017) 1-23.

[3] Y. Zhang, W. Guo, Y. Li, H. Chi, P. Zhao, K. Tagawa, An experimental study of icing distribution on a symmetrical airfoil for wind turbine blade in the offshore environmental condition, Ocean Engineering, 273 (2023) 113960.

[4] S. Gong, W. Chen, C. Zhang, Q. Yan, H. Yang, Variability of Sea Ice from 2008 to 2019 in the Bohai and Northern Huanghai Sea, China and the Relationship with Climatic Factors, Journal of Ocean University of China, 21 (2022) 1189-1197.

[5] Z. Liao, S. Dong, S. Tao, Y. Hua, N. Jia, Joint Probability Analysis and Prediction of Sea Ice Conditions in Liaodong Bay, Journal of Ocean University of China, 23 (2024) 57-68.

[6] I. Janajreh, H. Zhang, K. El Kadi, N. Ghaffour, Freeze desalination: Current research development and future prospects, Water Research, 229 (2023) 119389.

[7] L. Yang, U. Villalobos, B. Akhmetov, A. Gil, J.O. Khor, A. Palacios, Y. Li, Y. Ding, L.F. Cabeza, W.L. Tan, A. Romagnoli, A comprehensive review on sub-zero temperature cold thermal energy storage materials, technologies, and applications: State of the art and recent developments, Applied Energy, 288 (2021) 116555.

[8] B. Kalista, H. Shin, J. Cho, A. Jang, Current development and future prospect review of freeze desalination, Desalination, 447 (2018) 167-181.

[9] M.C. Barma, Z. Peng, B. Moghtaderi, E. Doroodchi, Freeze desalination of drops of saline solutions, Desalination, 517 (2021).

[10] A.L. Yarin, Drop impact dynamics: splashing, spreading, receding, bouncing., in: Annual review of fluid mechanics., 2006, pp. 159--192.

[11] L. Chen, Z. Xiao, P.C.H. Chan, Y.-K. Lee, Z. Li, A comparative study of droplet impact dynamics on a dual-scaled superhydrophobic surface and lotus leaf, Applied Surface Science, 257 (2011) 8857-8863.

[12] B. Asai, H. Tan, A.U. Siddique, Droplet Impact on a Micro-structured Hydrophilic Surface: Maximum Spreading, Jetting, and Partial Rebound, International Journal of Multiphase Flow, 157 (2022) 104235.

[13] L. Xiao, G.-M. Gou, S.-Y. Wu, J. Luo, Y. Xiang, Effect of incident direction and droplet position on dynamic and heat transfer behaviors of droplet impacting on super-hydrophilic cylindrical surface, Annals of Nuclear Energy, 187 (2023) 109785.

[14] K.A. Raman, R.K. Jaiman, T.-S. Lee, H.-T. Low, Lattice Boltzmann simulations of droplet impact onto surfaces with varying wettabilities, International Journal of Heat and Mass Transfer, 95 (2016) 336-354.

[15] E. Ezzatneshan, A. Khosroabadi, Droplet spreading dynamics on hydrophobic textured surfaces: A lattice Boltzmann study, Computers & Fluids, 231 (2021) 105063.
[16] A. Ashrafi-Habibabadi, A. Moosavi, Droplet condensation and jumping on structured superhydrophobic surfaces, International Journal of Heat and Mass Transfer, 134 (2019) 680-693.
[17] Y. Hou, H. Deng, Q. Du, K. Jiao, Multi-component multi-phase lattice Boltzmann modeling of droplet coalescence in flow channel of fuel cell, Journal of Power Sources, 393 (2018) 83-91.
[18] R.G.M. van der Sman, Multiscale simulations of directional ice crystal growth in sugar solutions, Food Structure, 30 (2021) 100214.
[19] S. Luo, Y. Jin, R. Tao, H. Li, C. Li, J. Wang, Z. Li, Molecular understanding of ion rejection in the freezing of aqueous solutions, Physical Chemistry Chemical Physics, 23 (2021) 13292-13299.
[20] C. Zhao, Y. Lin, X. Wu, X. Zhang, F. Chu, Nanoscale insights on the freezing front propagation and ion behaviors during seawater freezing, Applied Surface Science, 641 (2023) 158499.
[21] C. Zhao, Z. Hu, Y. Lin, X. Wu, X. Zhang, F. Chu, Effects of salinity and temperature on the icing of sessile saltwater droplets on solid surfaces, Desalination, 591 (2024).
[22] A. Eghtesad, M. Salakhi, H. Afshin, S.K. Hannani, Numerical investigation and optimization of indirect freeze desalination, Desalination, 481 (2020) 114378.
[23] T. Takaki, Phase-field Modeling and Simulations of Dendrite Growth, Transactions of the Iron & Steel Institute of Japan 52 (2014) 437-444.
[24] X. Wang, H. Zhang, W. Zhou, J. Ouyang, A 3D phase-field model for simulating the crystal growth of semi-crystalline polymers, International Journal of Heat and Mass Transfer, 115 (2017) 194-205.
[25] H. Yuan, K. Sun, K. Wang, J. Zhang, Z. Zhang, L. Zhang, S. Li, Y. Li, Ice crystal growth in the freezing desalination process of binary water-NaCl system, Desalination, 496 (2020) 114737.
[26] J. Song, D. Zhang, H. Yuan, J. Zhang, P. Zhou, Y. Li, K. Wang, N. Mei, Sea water frozen crystalisation impacted by flow and heterogeneous nucleation: PFM-LBM coupled modeling, simulation and experiments, Desalination, 524 (2022) 115484.
[27] K. Wang, D. Zhang, N. Mei, J. Zhang, Y. Li, H. Si, H. Yuan, Inhibition effect of adsorption on brine pockets formation during seawater freeze desalination, Desalination, 526 (2022) 115507.
[28] R. Song, K. Wang, M. Gong, H. Yuan, Multi-physical field simulations of directional seawater freeze-crystallisation under a magnetic field, Desalination, 560 (2023) 116687.
[29] J.H. Snoeijer, P. Brunet, Pointy ice-drops: How water freezes into a singular shape, American Journal of Physics, 80 (2012) 764-771.
[30] X.L. Yuheng Shang, Bofeng Bai, Xin Zhong, Central-pointy to central-concave icing transition of an impact droplet by increasing surface subcooling., International Communications in Heat and Mass Transfer, 108 (2019) 104326.
[31] X. Liu, Y. Guo, J. Min, X. Zhang, X. Wu, Impact and freezing coupling processes of supercooled water droplets on cold superhydrophobic spheres at low Weber numbers, Applied Thermal Engineering, 236 (2024) 121692.
[32] Y. Shang, B. Bai, Y. Hou, X. Zhong, L. Sun, Alteration of freezing paradigms of an impact water droplet on different cold surfaces, International Journal of Heat and Mass Transfer, 183 (2022) 122177.
[33] W.-Z. Fang, F.-Q. Zhu, F. Shen, D. Chai, W.-Q. Tao, Freezing behaviors of impacting water droplets on cold inclined surfaces, Applied Thermal Engineering, 219 (2023) 119562.
[34] Alizadeh Azar, Vaibhav Bahadur, Sheng Zhong, Wen Shang, Ri Li, James Ruud, Masako Yamada, Liehui Ge, Ali Dhinojwala, M. Sohal., Temperature Dependent Droplet Impact Dynamics on Flat and

Texture, Applied physics letters, 100 (2012) 111601.
[35] H. Lin, Z. Jin, Z. Yang, Y. Wu, The impact and freezing processes of a saltwater droplet on an ice surface, Physics of Fluids, 36 (2024).
[36] Y. Wang, L. Ju, D. Han, Q. Wang, Numerical investigation of the impacting and freezing process of a single supercooled water droplet, Physics of Fluids, 33 (2021) 042114.
[37] Z. Ma, W. Xiong, P. Cheng, 3D Lattice Boltzmann simulations for water droplet's impact and transition from central-pointy icing pattern to central-concave icing pattern on supercooled surfaces. Part I: Smooth surfaces, International Journal of Heat and Mass Transfer, 171 (2021) 121097.
[38] X. Zhang, K. Li, Z. Zhu, W.-Z. Fang, F.-Q. Zhu, C. Yang, Droplet impact and freezing dynamics on ultra-cold surfaces: A scaling analysis of central-concave pattern, Applied Thermal Engineering, 239 (2024) 122135.
[39] F. Chu, S. Li, C. Zhao, Y. Feng, Y. Lin, X. Wu, X. Yan, N. Miljkovic, Interfacial ice sprouting during salty water droplet freezing, Nature Communications, 15 (2024) 2249.
[40] P. Lallemand, L.S. Luo, Theory of the lattice Boltzmann method: Dispersion, dissipation, isotropy, Galilean invariance, and stability, Physical Review E, 61 (2000) 6546-6562.
[41] H. Deng, K. Jiao, Y. Hou, J.W. Park, Q. Du, A lattice Boltzmann model for multi-component two-phase gas-liquid flow with realistic fluid properties, International Journal of Heat and Mass Transfer, 128 (2019) 536-549.
[42] W. Xiong, P. Cheng, Numerical investigation of air entrapment in a molten droplet impacting and solidifying on a cold smooth substrate by 3D lattice Boltzmann method, International Journal of Heat and Mass Transfer, 124 (2018) 1262-1274.
[43] J. Wang, L. Wang, J. Huang, D. Li, Droplet impact behavior on a hydrophobic plate with a wettability-patterned orifice: A lattice Boltzmann study, International Communications in Heat and Mass Transfer, 159 (2024).
[44] Q. Li, K.H. Luo, Achieving tunable surface tension in the pseudopotential lattice Boltzmann modeling of multiphase flows, Physical Review E, 88 (2013) 053307.
[45] C.D. Stiles, Y. Xue, High density ratio lattice Boltzmann method simulations of multicomponent multiphase transport of H2O in air, Computers & Fluids, 131 (2016) 81-90.
[46] Q. Li, K.H. Luo, X.J. Li, Lattice Boltzmann modeling of multiphase flows at large density ratio with an improved pseudopotential model, Physical Review E, 87 (2013) 053301.
[47] K.W.T. Kim S G , Suzuki T Phase-field model for binary alloys, Physical Review E Statistical Physics Plasmas Fluids & Related Interdisciplinary Topics, 60 (1999) 7186.
[48] G. Demange, H. Zapolsky, R. Patte, M. Brunel, A phase field model for snow crystal growth in three dimensions, NPJ COMPUTATIONAL MATERIALS, 3:15 (2017) 1-7.
[49] A.A. Wheeler, W.J. Boettinger, G.B. McFadden, Phase-field model for isothermal phase transitions in binary alloys, Physical Review A, 45 (1992) 7424-7439.
[50] H. Dong, W.W. Carr, D.G. Bucknall, J.F. Morris, Temporally-resolved inkjet drop impaction on surfaces, AIChE Journal, 53 (2007) 2606-2617.
[51] J. Huang, L. Wang, K. He, Three-dimensional study of double droplets impact on a wettability-patterned surface, Computers & Fluids, 248 (2022).
[52] A.R. Dehghani-Sanij, S.R. Dehghani, G.F. Naterer, Y.S. Muzychka, Sea spray icing phenomena on marine vessels and offshore structures: Review and formulation, Ocean Engineering, 132 (2017) 25-39.
[53] G. Demange, H. Zapolsky, R. Patte, M. Brunel, Growth kinetics and morphology of snowflakes in supersaturated atmosphere using a three-dimensional phase-field model, PHYSICAL REVIEW E, 96

(2017) 022803.

[54] A. Poisson, A. Papaud, Diffusion coefficients of major ions in seawater., Marine Chemistry, 13 (1983) 280.

Credit Author Statement

Xinyu Liu: Software, Data curation, Writing-original draft, Visualization.

Han Yuan: Conceptualization, Methodology, Supervision, Writing-review & editing, Funding acquisition.

Yuan Zhao: Investigation, Data curation, Visualization.

Ji Zhang: Investigation, Project administration, Funding acquisition.

Haibin Wang: Supervision, Investigation.

Declaration of interests

☐ The authors declare that they have no known competing financial interests or personal relationships that could have appeared to influence the work reported in this paper.

☒The authors declare the following financial interests/personal relationships which may be considered as potential competing interests: